AGU PUBLICATIONS

JGR

Journal of Geophysical Research: Solid Earth

RESEARCH ARTICLE
10.1002/2016JB013882

Special Section:
Rock Physics of the Upper Crust

Rock anelasticity due to patchy saturation and fabric heterogeneity: A double double-porosity model of wave propagation

Jing Ba[1,2], Wenhao Xu[2], Li-Yun Fu[3], José M. Carcione[4], and Lin Zhang[1]

[1]School of Earth Sciences and Engineering, Hohai University, Nanjing, China, [2]Department of Computational Geophysics, Xi'an Jiaotong University, Xi'an, China, [3]Institute of Geology and Geophysics, Chinese Academy of Sciences, Beijing, China, [4]Istituto Nazionale di Oceanografia e di Geofisica Sperimentale, Trieste, Italy

Key Points:
- A double double-porosity theory is presented for wave anelasticity by analyzing the overlapping effect of fluid and fabric heterogeneities
- Modeling and experimental data show strong multifrequency dispersion and attenuation associated with fabric heterogeneity scales
- Fluid-heterogeneity scale and characteristic frequency of peak attenuation are correlated to rock fabric heterogeneity size

Correspondence to:
J. Ba,
baj04@mails.tsinghua.edu.cn;
jba@hhu.edu.cn

Citation:
Ba, J., W. Xu, L.-Y. Fu, J. M. Carcione, and L. Zhang (2017), Rock anelasticity due to patchy saturation and fabric heterogeneity: A double double-porosity model of wave propagation, *J. Geophys. Res. Solid Earth*, *122*, 1949–1976, doi:10.1002/2016JB013882.

Received 20 DEC 2016
Accepted 4 MAR 2017
Accepted article online 7 MAR 2017
Published online 23 MAR 2017

Abstract Heterogeneity of rock's fabric can induce heterogeneous distribution of immiscible fluids in natural reservoirs, since the lithological variations (mainly permeability) may affect fluid migration in geological time scales, resulting in patchy saturation of fluids. Therefore, fabric and saturation inhomogeneities both affect wave propagation. To model the wave effects (attenuation and velocity dispersion), we introduce a double double-porosity model, where pores saturated with two different fluids overlap with pores having dissimilar compressibilities. The governing equations are derived by using Hamilton's principle based on the potential energy, kinetic energy, and dissipation functions, and the stiffness coefficients are determined by gedanken experiments, yielding one fast *P* wave and four slow Biot waves. Three examples are given, namely, muddy siltstones, clean dolomites, and tight sandstones, where fabric heterogeneities at three different spatial scales are analyzed in comparison with experimental data. In muddy siltstones, where intrapore clay and intergranular pores constitute a submicroscopic double-porosity structure, wave anelasticity mainly occurs in the frequency range (10^4–10^7 Hz), while in pure dolomites with microscopic heterogeneity of grain contacts and tight sandstones with mesoscopic heterogeneity of less consolidated sands, it occurs at 10^3–10^7 Hz and 10^1–10^3 Hz (seismic band), respectively. The predicted maximum quality factor of the fast compressional wave for the sandstone is the lowest (approximately 8), and that of the dolomite is the highest. The results of the diffusive slow waves are affected by the strong friction effects between solids and fluids. The model describes wave propagation in patchy-saturated rocks with fabric heterogeneity at different scales, and the relevant theoretical predictions agree well with the experimental data in fully and partially saturated rocks.

Plain Language Summary Wave-induced local fluid flow is widely accepted as the main cause of compressional wave anelasticity (velocity dispersion and attenuation) in fluid-saturated rocks. The two intrinsic causes of wave-induced local fluid flow, rock fabric and fluid patchy saturation, were discussed and analyzed frequently in the literature. However, their combination in one single theory results in much complex geometries, and no poroelasticity theory has been presented so far. In natural tight rocks, the two types of heterogeneities (rock fabric and fluid distribution) generally coexist, since low permeability and capillary forces hinder fluid migration and induce patchy saturation. The exact theoretical equations for wave propagation in this type of medium will provide an important basis for further rock physics studies and field applications of seismic exploration. New theoretical equations are derived by proposing a double double-porosity model and incorporating the two types of heterogeneities into the same set of equations under the framework of Biot poroelasticity. We compare the theory with three sets of experimental data, which contain heterogeneities at the different scales. The model successfully describes wave propagation in patchy-saturated rocks with fabric heterogeneity at different scales, allowing for the most comprehensive description of compressional wave propagation and dissipation characteristics in highly complex in situ reservoir rocks.

1. Introduction

It is widely accepted that the intrinsic anelasticity of sedimentary rocks, where significant wave-velocity dispersion and attenuation are observed at different frequencies [*King and Marsden*, 2002; *Batzle et al.*, 2006; *Best et al.*, 2013; *Adam and Otheim*, 2013; *Tisato and Quintal*, 2014; *Ba et al.*, 2016; *Spencer and Shine*, 2016], is mainly caused by wave-induced local fluid flow mechanisms (WILFF) [*Dvorkin et al.*, 1994; *Johnson*, 2001; *Pride et al.*, 2004; *Ba et al.*, 2011; *Carcione and Gurevich*, 2011]. Two types of WILFF are discussed in the literature. The first is rock fabric heterogeneity, where the compressibility contrast between different pore

systems induces fluid flow under compressional wave oscillations. Flow from softer pores to stiff pores when wave squeezes the rock skeleton, causes wave relaxation at characteristic frequencies, resulting in wave velocity increasing with frequency and related intrinsic attenuation (the WILFF and anelasticity associated with rock fabric is indicated as Type I in this work). Patchy saturation of immiscible fluids also accounts for wave anelasticity, where a pressure gradient is induced between rock skeletons with the same compressibility saturated with different fluids. Strong attenuation is observed when the compressibility contrast is high between the fluids [*Müller et al*., 2010; *Ba et al*., 2015b] (here anelasticity associated with patchy saturation is denoted as Type II). In this work, we investigate the combined effects of rock-fabric heterogeneity and patchy saturation on wave propagation, since these two types of heterogeneity coexist in natural reservoirs, especially in the low-permeability tight rocks, where capillary forces in narrow pore throats hinder the migration of light gas and hydrocarbons, causing heterogeneous distribution of fluids, i.e., rock fabric consequently induces patchy saturation.

The studies on Type-I anelasticity started with *Mavko and Nur* [1975]. They presented a model of a liquid-filled flat crack, where melt squirt flow occurs in wave oscillations, accounting for wave loss and velocity decrease in the asthenosphere. A microscopic model was first proposed [*Mavko and Nur*, 1978, 1979] where WILFF occurs in microcracks and produces much higher attenuation than that of the Biot theory [*Biot*, 1956], being capable of explaining the observed experimental data. A unified model of Biot/squirt (BISQ) equations has been derived by *Dvorkin and Nur* [1993], where the Biot friction between the grains and the pore fluid and the squirt flow occurring between grain contacts/cracks and the main pore cavity is incorporated in the same poroelasticity equations. The BISQ model regards the microscopic scale, since the flow does not exceed the average diameter of the mineral grains, approximately 10 μm to several 100 μm.

An extended study is proposed by *Chapman* [2003] to describe wave-induced fluid flow in fractures at a larger scale than the grain size, which agrees with experimental results in the low-frequency limit. *Pride et al*. [2004] presented the governing equations for wave propagation in double-porosity medium to describe the WILFF in rocks with mesoscopic heterogeneities. The inhomogeneities with a size larger than the grain diameter but much smaller than the seismic wavelength are assumed to be embedded in a host skeleton with different compressibility, causing strong attenuation at seismic frequencies. *Ba et al*. [2011, 2014] derived a set of exact equations for wave propagation in double-porosity rocks containing mesoscopic heterogeneities, the so called Biot-Rayleigh (BR) equations, where a bubble oscillation equation [*Rayleigh*, 1917] is extended and incorporated to the poroelasticity equations to model a WILFF kinetic energy in the Biot theoretical framework.

In addition to mesoscopic and microscopic models for rock fabric heterogeneity, the clay squirt flow mechanism has been discussed by *Best and McCann* [1995], where WILFF occurs between micropores of intrapore clay and intergranular macropores, suggesting a submicroscopic double-porosity structure since the micropores in clay aggregates are much smaller than the size of the grains, generally smaller than 1 μm and approximately with a size of several hundred nanometers. Recently, several models have been successfully applied to model the clay squirt flow mechanism in shaly/muddy rocks [*Best et al*., 2013; *Marketos and Best*, 2010; *Ba et al*., 2016].

White [1975] first investigated the Type-II wave anelasticity by proposing a patchy-saturation model where a spherical gas pocket is embedded in a concentric spherical shell (water saturated). *Dutta and Odé* [1979] reformulated White's equations under the framework of the poroelasticity theory, and their equations are mathematically exact and more rigorous. *Pride et al*. [2004] first used the double-porosity governing equations to model the mesoscopic loss caused by patchy saturation of immiscible fluids. The model they considered is equivalent to White's model. *Ba et al*. [2012, 2015b] extended the BR theory from the case of a composite saturated with a single fluid to the case of a single lithology saturated with two different fluids, where the inclusions, a porous continuum saturated with a second type of fluid, are assumed spherical.

Another mesoscopic geometrical model of patchy saturation, the horizontal periodic alternative layered model, is presented by *White et al*. [1975]. Each layer of porous medium is saturated with a different type of fluid with the upper and lower adjacent layers. The interval between the two central points of the two adjacent layers which are saturated with different fluids is analyzed as a unit volume. The incident plane wave is assumed perpendicular to the layer interfaces, and the results are obtained based on a 1-D theoretical analysis; therefore, the model is actually a 1-D model. *Norris* [1993] presents a more exact approach by using the Biot's poroelasticity theory to analyze low-frequency wave anelasticity in the periodic 1-D model of

partially saturated rocks. *Gurevich and Lopatnikov* [1995] also used the poroelasticity theory, and they further considered a random alternative layered medium.

Johnson [2001] presented a theory which allows for an arbitrary geometry of the patches. In the work, a branching equation is used to relate the low- and high-frequency limits of the complex bulk modulus. *Pride et al*. [2004] also used the branching equation in their double-porosity theory; however, they only modeled spherical gas pockets. More complicated geometries are considered by *Ciz et al*. [2006] to model randomly distributed sphere patches. The 1-D and 3-D continuous random models are presented by *Gurevich and Lopatnikov* [1995] and *Müller and Gurevich* [2005], respectively. The works related to this topic were reviewed by *Müller et al*. [2010]. *Sun et al*. [2015] systematically analyzed the previous theoretical models in which different geometries are considered and different approaches are applied, based on numerical examples with the same set of input rock properties as well as comparing the theoretical prediction results with laboratory data.

Theoretical models of Type-II anelasticity (patchy saturation) consider the mesoscopic scale. Patches/pockets saturated with immiscible fluids are considered to be larger than the average grain/pore size according to *Caspari et al*. [2011] (for sandstone) and *Lopes et al*. [2014] (for carbonate). However, in mudstones, shales, and siltstones with much smaller grains and extremely low permeability, the fluid pockets may be smaller than intergranular pores.

The two types of heterogeneity (rock's fabric and patchy saturation) commonly coexist in natural rocks. The pore-structure effects on the actual fluid distribution, especially for tight and dense rocks, where low permeability and capillary forces of pore throats affect fluid migration, further strengthen the heterogeneity of the second type. The overlapping effect of the two heterogeneities on rock anelasticity (denoted by Type III) is very common in shallow rocks. This effect has been investigated in *Ba et al*. [2015a] by proposing a "double double-porosity" (DDP) poroelasticity model, where patchy saturation occurs in each porous continuum of a primary double-porosity solid. Therefore, the two sets of pores saturated with different fluids constitute a secondary double-porosity structure, representing a quadruple-porosity system. A simplified model is presented by *Sun et al*. [2016], where patchy saturation in the host medium is neglected (compared to the DDP theory) and a triple-layer patchy is assumed with a triple-layer concentric sphere (inner core, middle shell, and outer shell with different pore fluids and/or solid skeletons, similar to the triple-porosity theory presented by *Zhang et al*. [2017] for a mud, sand, and conglomerate mixture). Beside poroelasticity theories, a pure numerical approach is applied by *Rubino and Holliger* [2012] which takes into account heterogeneities associated with the dry frame properties as well as spatial variations of the pore fluid properties. They concluded from numerical results that the seismic responses with regard to attenuation and phase velocity are more sensitive to the heterogeneities associated with the fluid properties than to solid frame and, therefore, rock frame heterogeneities, which do not significantly affect the seismic responses per se. *Quintal et al*. [2012] numerically investigated the attenuation and dispersion of *S* waves in a double-porosity media with patchy saturation and suggested that *S* wave attenuation could be used as an indicator of fluid content in a reservoir.

In this work, we present the double double-porosity theory for wave propagation in a heterogeneous rock. The governing equations of Type-III anelasticity are obtained from Hamilton's principle, by deriving the strain potential energy, kinetic energy, and dissipation functions based on the BR theoretical framework. Then, we determine the elastic, density, and dissipation coefficients based on gedanken experiments. The wave equations are solved by substituting a plane-wave analytical kernel. Three rock experimental data sets are selected in examples, according to the fabric heterogeneity at three different scales (muddy siltstones with submicroscopic heterogeneity, carbonates with microscopic heterogeneity, and sandstone with mesoscopic heterogeneity, respectively), and we present numerical examples and predict the compressional wave velocities at different conditions, in comparison with the experimental data. Finally, we summarize the results of these modeling and comparative analyses.

2. Double Double-Porosity Theory for Wave Propagation

Consider a double-porosity medium, where each porous component is patchy saturated, with porosity ϕ_{10} the host skeleton and porosity ϕ_{20} the inclusion skeleton. The total rock porosity is $\phi = \phi_{10}v_1 + \phi_{20}v_2$, where v_1 and v_2 are the volume contents of the two porous components, with $v_1 + v_2 = 1$. Each component can mathematically be treated as a double-porosity medium at a smaller scale, by considering pores saturated

with the host fluid (with density $\rho_f^{(1)}$, viscosity $\eta_f^{(1)}$, and bulk modulus $K_f^{(1)}$) and inclusion fluid (with density $\rho_f^{(2)}$, viscosity $\eta_f^{(2)}$, and bulk modulus $K_f^{(2)}$) as two different pore types (for instance, "gas-saturated pores" and "water-saturated pores" in a rock partially saturated with gas and water), since pore-fluid changes will result in compressibility and density variations of the whole solid-fluid composite. This quadruple-porosity system has four absolute porosities, $\phi_1 = v_1\phi_{10}S_1$ (host skeleton and host fluid), $\phi_3 = v_1\phi_{10}(1 - S_1)$ (host skeleton and inclusion fluid), $\phi_2 = v_2\phi_{20}S_2$ (inclusion skeleton and host fluid), and $\phi_4 = v_2\phi_{20}(1 - S_2)$ (inclusion skeleton and inclusion fluid), where S_1 and S_2 are the saturations of the host fluids in the two components (generally, we assume that the host and inclusion skeletons share the same host fluid). Rock's fabric heterogeneity geometrically overlaps with patchy saturation in the DDP model proposed here.

2.1. Strain Potential Energy, Kinetic Energy, and Dissipation Equations

When compressional waves squeeze the double double-porosity system described above, local fluid flow occurs at the three sets of interfaces, the interface between fluids in the host medium (Type II), the interface between fluids in the inclusions (Type II), and the interface between the inclusion skeleton and the host skeleton (Type I), since the two phases at each interface have different compressibilities. There is a coupling effect from the three sets of WILFF under the periodic oscillations of compressional waves generating the Type-III anelasticity. We define four independent fluid-displacement vectors $\mathbf{U}^{(m)} = \left[U_1^{(m)}, U_2^{(m)}, U_3^{(m)}\right], m = 1,2,3,4$ (which correspond to the four porosities ϕ_m) to simulate the dynamic process of the Type-III WILFF, and the solid-displacement vector $\mathbf{u} = [u_1, u_2, u_3]$. The time variable is denoted by t and the spatial variables by x_1, x_2, and x_3, while the strain components of the solid and fluid components are as follows:

$$e_{ij} = \frac{1}{2}\left(\frac{\partial u_i}{\partial x_j} + \frac{\partial u_j}{\partial x_i}\right) \text{ and } \xi_{ij}^{(m)} = \frac{1}{2}\left(\frac{\partial U_i^{(m)}}{\partial x_j} + \frac{\partial U_j^{(m)}}{\partial x_i}\right), \tag{1}$$

with the dilatations that are defined as follows:

$$e = e_{ii} = \frac{\partial u_i}{\partial x_i} \text{ and } \xi^{(m)} = \xi_{ii}^{(m)} = \frac{\partial U_i^{(m)}}{\partial x_i} \tag{2}$$

(the Einstein summation of repeated indices is assumed).

In the framework of Biot's poroelasticity theory, the strain energy in a double double-porosity medium is a function of seven independent variables (three for the solid skeleton and four for the pore phases):

$$\begin{aligned} 2W = (A + 2N)I_1^2 - 4NI_2 + 2Q_1I_1\xi_1 + R_1\xi_1^2 + 2Q_3I_1\xi_3 + R_3\xi_3^2, \\ + 2Q_2I_1\xi_2 + R_2\xi_2^2 + 2Q_4I_1\xi_4 + R_4\xi_4^2 \end{aligned} \tag{3}$$

where A, N, Q, and R are the Biot stiffness coefficients and

$$I_1 = e, \quad I_2 = \begin{vmatrix} e_{11} & e_{12} \\ e_{12} & e_{22} \end{vmatrix} + \begin{vmatrix} e_{22} & e_{23} \\ e_{23} & e_{33} \end{vmatrix} + \begin{vmatrix} e_{33} & e_{13} \\ e_{13} & e_{11} \end{vmatrix} \text{ and } I_3 = \begin{vmatrix} e_{11} & e_{12} & e_{13} \\ e_{12} & e_{22} & e_{23} \\ e_{13} & e_{23} & e_{33} \end{vmatrix}.$$

Based on the BR theory [*Ba et al.*, 2011], the relaxation effect of WILFF at the three sets of interfaces can be incorporated into the strain potential equation by introducing three independent fluid increments, ζ_{12}, ζ_{13}, and ζ_{24}, where the subscripts 12, 13, and 24 denote the fluid strain increments in the coupled WILFF process crossing the interfaces between phase 1 and phase 2 (ϕ_1 and ϕ_2), phase 1 and phase 3 (ϕ_1 and ϕ_3), and phase 2 and phase 4 (ϕ_2 and ϕ_4). Oscillations of WILFF occur at the interfaces, and pore fluid strains are relaxed at each interface between different phases, before potential energy is transferred to kinetic energy in each wave period. The reformulated strain energy is as follows:

$$\begin{aligned} 2W = (A + 2N)I_1^2 - 4NI_2 + 2Q_1I_1(\xi_1 + \phi_2\zeta_{12} + \phi_3\zeta_{13}) + R_1(\xi_1 + \phi_2\zeta_{12} + \phi_3\zeta_{13})^2 \\ + 2Q_2I_1(\xi_2 - \phi_1\zeta_{12} + \phi_4\zeta_{24}) + R_2(\xi_2 - \phi_1\zeta_{12} + \phi_4\zeta_{24})^2 + 2Q_3I_1(\xi_3 - \phi_1\zeta_{13}) \\ + R_3(\xi_3 - \phi_1\zeta_{13})^2 + 2Q_4I_1(\xi_4 - \phi_2\zeta_{24}) + R_4(\xi_4 - \phi_2\zeta_{24})^2. \end{aligned} \tag{4}$$

According to the theories of *Biot* [1962] for a single-porosity solid and *Ba et al.* [2011] for a double-porosity solid, the kinetic energy for a double double-porosity medium can similarly be written as follows:

$$2T = \rho_{00}\sum_i \dot{u}_i^2 + 2\sum_m \rho_{0m}\sum_i \dot{u}_i\dot{U}_i^{(m)} + \sum_m \rho_{mm}\sum_i \left(\dot{U}_i^{(m)}\right)^2 \tag{5}$$

where ρ_{00}, ρ_{0m}, and ρ_{mm} are density coefficients.

The kinetic energy of the WILFF process is derived by assuming the unique sphere inclusions in a porous host medium in the double-porosity theory and establishing the analytical relation between the sphere radius and the fluid increment [*Ba et al.*, 2011]. For the double double-porosity model, we also assume the unique sphere inclusions of the second type of skeleton (with a radius R_{12}) embedded in the host solid skeleton, both of which are saturated with two immiscible fluids and share the same host fluid and inclusion fluid. All the pockets of inclusion fluid are assumed spherical, with a radius of R_{13} and R_{24} ($R_{24} << R_{12}$) for the inclusion skeleton and the host skeleton, respectively. We assume that the distance between the two inclusions is large, so that we neglect the interaction between the different inclusions.

Based on BR theory, the sum of the kinetic energy of WILFF from the three sets of interfaces is then derived as follows:

$$2T_L = \frac{1}{3}\rho_f^{(1)}\dot{\zeta}_{12}^2 R_{12}^2 \frac{\phi_1^2\phi_2^2\phi_{20}}{\phi_{10}(\phi_2+\phi_4)} + \frac{1}{3}\rho_f^{(1)}\dot{\zeta}_{13}^2 R_{13}^2\phi_1^2\phi_3 + \frac{1}{3}\rho_f^{(1)}\dot{\zeta}_{24}^2 R_{24}^2\phi_2^2\phi_4, \tag{6}$$

and the kinetic energy of the whole system is as follows:

$$\begin{aligned} 2T = {} & \rho_{00}\sum_i \dot{u}_i^2 + 2\sum_m \rho_{0m}\sum_i \dot{u}_i\dot{U}_i^{(m)} + \sum_m \rho_{mm}\sum_i \left(\dot{U}_i^{(m)}\right)^2 \\ & + \frac{1}{3}\rho_f^{(1)}\dot{\zeta}_{12}^2 R_{12}^2 \frac{\phi_1^2\phi_2^2\phi_{20}}{\phi_{10}(\phi_2+\phi_4)} + \frac{1}{3}\rho_f^{(1)}\dot{\zeta}_{13}^2 R_{13}^2\phi_1^2\phi_3 + \frac{1}{3}\rho_f^{(1)}\dot{\zeta}_{24}^2 R_{24}^2\phi_2^2\phi_4. \end{aligned} \tag{7}$$

The generalization of the Biot dissipation function accounting for the friction effect between the solid frame (with permeabilities κ_1 and κ_2 for the host skeleton and inclusion skeleton, respectively) and the pore fluid is here equal to

$$2D = \sum_m b_m\left(\mathbf{u} - \mathbf{U}^{(m)}\right)\cdot\left(\mathbf{u} - \mathbf{U}^{(m)}\right), \tag{8}$$

where the Biot dissipation coefficients are

$$b_1 = \phi_1\phi_{10}\frac{\eta_f^{(1)}}{\kappa_1}, \tag{9a}$$

$$b_2 = \phi_2\phi_{20}\frac{\eta_f^{(1)}}{\kappa_2}, \tag{9b}$$

$$b_3 = \phi_3\phi_{10}\frac{\eta_f^{(2)}}{\kappa_1}, \quad \textit{and} \tag{9c}$$

$$b_4 = \phi_4\phi_{20}\frac{\eta_f^{(2)}}{\kappa_2}. \tag{9d}$$

The additional dissipation from the three sets of WILFF process is obtained similar to the calculation of the kinetic energy T as

$$2D_L = \frac{1}{3}\eta_f^{(1)}\dot{\zeta}_{12}^2 R_{12}^2 \frac{\phi_1^2\phi_2^2\phi_{20}}{\kappa_1(\phi_2+\phi_4)} + \frac{1}{3}\eta_f^{(1)}\dot{\zeta}_{13}^2 R_{13}^2 \frac{\phi_3\phi_1^2\phi_{10}}{\kappa_1} + \frac{1}{3}\eta_f^{(1)}\dot{\zeta}_{24}^2 R_{24}^2 \frac{\phi_4\phi_2^2\phi_{20}}{\kappa_2}, \tag{10}$$

and the dissipation function of the whole system is finally

$$\begin{aligned} 2D = {} & \sum_m b_m\left(\mathbf{u} - \mathbf{U}^{(m)}\right)\cdot\left(\mathbf{u} - \mathbf{U}^{(m)}\right) + \frac{1}{3}\eta_f^{(1)}\dot{\zeta}_{12}^2 R_{12}^2 \frac{\phi_1^2\phi_2^2\phi_{20}}{\kappa_1(\phi_2+\phi_4)} \\ & + \frac{1}{3}\eta_f^{(1)}\dot{\zeta}_{13}^2 R_{13}^2 \frac{\phi_3\phi_1^2\phi_{10}}{\kappa_1} + \frac{1}{3}\eta_f^{(1)}\dot{\zeta}_{24}^2 R_{24}^2 \frac{\phi_4\phi_2^2\phi_{20}}{\kappa_2}. \end{aligned} \tag{11}$$

2.2. Governing Equations and Relevant Coefficients

Based on Hamilton's principle, the Lagrangian density of a conservative system is defined as $L = T - W$. By substituting the kinetic energy, the potential energy, and the dissipation function into the Lagrange equation, the governing equations of wave motion are derived with the solid and fluid displacements and the three fluid increments as generalized coordinates [*Ba et al.*, 2015a]:

$$\begin{aligned} &N\nabla^2\mathbf{u} + (A+N)\nabla e + Q_1\nabla\left(\xi^{(1)} + \phi_2\zeta_{12} + \phi_3\zeta_{13}\right) + Q_2\nabla\left(\xi^{(2)} - \phi_1\zeta_{12} + \phi_4\zeta_{24}\right) \\ &+Q_3\nabla\left(\xi^{(3)} - \phi_1\zeta_{13}\right) + Q_4\nabla\left(\xi^{(4)} - \phi_2\zeta_{24}\right) \\ &= \rho_{00}\ddot{\mathbf{u}} + \rho_{01}\ddot{\mathbf{U}}^{(1)} + \rho_{02}\ddot{\mathbf{U}}^{(2)} + \rho_{03}\ddot{\mathbf{U}}^{(3)} + \rho_{04}\ddot{\mathbf{U}}^{(4)} + b_1\left(\dot{\mathbf{u}} - \dot{\mathbf{U}}^{(1)}\right) + b_2\left(\dot{\mathbf{u}} - \dot{\mathbf{U}}^{(2)}\right) \\ &+b_3\left(\dot{\mathbf{u}} - \dot{\mathbf{U}}^{(3)}\right) + b_4\left(\dot{\mathbf{u}} - \dot{\mathbf{U}}^{(4)}\right), \end{aligned} \tag{12a}$$

$$Q_1\nabla e + R_1\nabla\left(\xi^{(1)} + \phi_2\zeta_{12} + \phi_3\zeta_{13}\right) = \rho_{01}\ddot{\mathbf{u}} + \rho_{11}\ddot{\mathbf{U}}^{(1)} - b_1\left(\dot{\mathbf{u}} - \dot{\mathbf{U}}^{(1)}\right), \tag{12b}$$

$$Q_2\nabla e + R_2\nabla\left(\xi^{(2)} - \phi_1\zeta_{12} + \phi_4\zeta_{24}\right) = \rho_{02}\ddot{\mathbf{u}} + \rho_{22}\ddot{\mathbf{U}}^{(2)} - b_2\left(\dot{\mathbf{u}} - \dot{\mathbf{U}}^{(2)}\right), \tag{12c}$$

$$Q_3\nabla e + R_3\nabla\left(\xi^{(3)} - \phi_1\zeta_{13}\right) = \rho_{03}\ddot{\mathbf{u}} + \rho_{33}\ddot{\mathbf{U}}^{(3)} - b_3\left(\dot{\mathbf{u}} - \dot{\mathbf{U}}^{(3)}\right), \tag{12d}$$

$$Q_4\nabla e + R_4\nabla\left(\xi^{(4)} - \phi_2\zeta_{24}\right) = \rho_{04}\ddot{\mathbf{u}} + \rho_{44}\ddot{\mathbf{U}}^{(4)} - b_4\left(\dot{\mathbf{u}} - \dot{\mathbf{U}}^{(4)}\right), \tag{12e}$$

$$\begin{aligned} &\phi_2\left(Q_1 e + R_1\left(\xi^{(1)} + \phi_2\zeta_{12} + \phi_3\zeta_{13}\right)\right) - \phi_1\left(Q_2 e + R_2\left(\xi^{(2)} - \phi_1\zeta_{12} + \phi_4\zeta_{24}\right)\right) \\ &= \frac{1}{3}\rho_f^{(1)}\ddot{\zeta}_{12}R_{12}^2\frac{\phi_1^2\phi_2^2\phi_{20}}{\phi_{10}(\phi_2+\phi_4)} + \frac{1}{3}\dot{\zeta}_{12}R_{12}^2\frac{\eta_f^{(1)}\phi_1^2\phi_2^2\phi_{20}}{\kappa_1(\phi_2+\phi_4)}, \end{aligned} \tag{12f}$$

$$\begin{aligned} &\phi_3\left(Q_1 e + R_1\left(\xi^{(1)} + \phi_2\zeta_{12} + \phi_3\zeta_{13}\right)\right) - \phi_1\left(Q_3 e + R_3\left(\xi^{(2)} - \phi_1\zeta_{13}\right)\right) \\ &= \frac{1}{3}\rho_f^{(1)}\ddot{\zeta}_{13}R_{13}^2\phi_1^2\phi_3 + \frac{1}{3}\dot{\zeta}_{13}R_{13}^2\frac{\eta_f^{(1)}\phi_1^2\phi_3\phi_{10}}{\kappa_1}, \text{ and} \end{aligned} \tag{12g}$$

$$\begin{aligned} &\phi_4\left(Q_2 e + R_2\left(\xi^{(2)} - \phi_1\zeta_{12} + \phi_4\zeta_{24}\right)\right) - \phi_2\left(Q_4 e + R_4\left(\xi^{(4)} - \phi_2\zeta_{24}\right)\right) \\ &= \frac{1}{3}\rho_f^{(1)}\ddot{\zeta}_{24}R_{24}^2\phi_2^2\phi_4 + \frac{1}{3}\dot{\zeta}_{24}R_{24}^2\frac{\eta_f^{(1)}\phi_2^2\phi_4\phi_{20}}{\kappa_2}. \end{aligned} \tag{12h}$$

The coupled equations have 10 stiffness coefficients and 9 density coefficients, all of which can be determined on the basis of the measurable properties of solid and fluids.

The calculation of the density coefficients follows *Biot* [1956] (for a single-porosity medium), *Ba et al.* [2011] (for a double-porosity model considering Type-I anelasticity), and *Sun et al.* [2015] (for a double-porosity model considering Type-II anelasticity):

$$\rho_{11} = \alpha_{10}\phi_1\rho_f^{(1)}, \tag{13a}$$

$$\rho_{22} = \alpha_{20}\phi_2\rho_f^{(1)}, \tag{13b}$$

$$\rho_{33} = \alpha_{10}\phi_3\rho_f^{(2)}, \tag{13c}$$

$$\rho_{44} = \alpha_{20}\phi_4\rho_f^{(2)}, \tag{13d}$$

$$\rho_{01} = \phi_1\rho_f^{(1)} - \rho_{11}, \tag{13e}$$

$$\rho_{02} = \phi_2\rho_f^{(1)} - \rho_{22}, \tag{13f}$$

$$\rho_{03} = \phi_3\rho_f^{(2)} - \rho_{33}, \tag{13g}$$

$$\rho_{04} = \phi_4\rho_f^{(2)} - \rho_{44}, \text{ and} \tag{13h}$$

$$\rho_{00} = (1-\phi)\rho_s - \rho_{01} - \rho_{02} - \rho_{03} - \rho_{04}, \tag{13i}$$

where ρ_s is the grain mass density and α_{10} and α_{20} are the tortuosities of the pores in the host skeleton and inclusion skeleton, which can be calculated as [*Ba et al.*, 2011] follows:

$$\alpha_{10} = 0.5\left(\frac{1}{\phi_{10}} + 1\right) \text{ and } \alpha_{20} = 0.5\left(\frac{1}{\phi_{20}} + 1\right). \tag{14}$$

The approach of gedanken experiments [*Johnson*, 1986] is used to establish the analytical relationships between the stiffness coefficients and the measurable properties of solid and fluids.

First of all, the stress-strain relation of constitutive equations can be derived as follows:

$$\tau_{ij} = \frac{\partial W}{\partial e_{ij}} \text{ and } \tau^{(m)} = \frac{\partial W}{\partial \xi_m}. \tag{15}$$

The following idealized experiments [*Biot and Willis*, 1957; *Ba et al*., 2011, 2015b] are performed in a double double-porosity model.

1. The rock model is subjected to a pure shear deformation. N is the shear modulus of the frame, since the fluid does not contribute to the shearing force. Therefore,

$$N = \mu_b, \tag{16}$$

where μ_b is the dry-rock shear modulus.

2. The rock is surrounded by a flexible rubber jacket, subjected to a hydrostatic pressure, and the pore fluid is allowed to flow in and out, which does not affect the rock deformation. Based on equation (15), we have

$$A + \frac{2}{3}N - \sum_m \frac{Q_m^2}{R_m} = K_b, \tag{17}$$

where K_b is the dry-rock skeleton bulk modulus.

3. An unjacketed rock sample is subjected to a hydrostatic pressure. Another five relations are derived from equation (15) as follows:

$$\frac{A + \frac{2}{3}N}{K_s} + \frac{Q_1}{K_f^{(1)}} + \frac{Q_2}{K_f^{(1)}} + \frac{Q_3}{K_f^{(2)}} + \frac{Q_4}{K_f^{(2)}} = 1 - \phi, \tag{18a}$$

$$\frac{Q_1}{K_s} + \frac{R_1}{K_f^{(1)}} = \phi_1, \tag{18b}$$

$$\frac{Q_2}{K_s} + \frac{R_2}{K_f^{(1)}} = \phi_2, \tag{18c}$$

$$\frac{Q_3}{K_s} + \frac{R_3}{K_f^{(2)}} = \phi_3, \text{ and} \tag{18d}$$

$$\frac{Q_4}{K_s} + \frac{R_4}{K_f^{(2)}} = \phi_4. \tag{18e}$$

4. An additional relation can be derived according to the double-porosity model for Type-I anelasticity. With β determined by the equation (40) of *Ba et al*. [2011], the dilatation ratio of fluid bulk strain between phases 1 and 2 yields

$$\frac{Q_1}{R_1} = \beta \frac{Q_2}{R_2}. \tag{19}$$

5. For Type-II local fluid flow between phases 1 and 3 (or phases 2 and 4), the two components at the fluid pocket boundary yield $\beta = 1$; therefore,

$$\frac{Q_3}{R_3} = \frac{Q_1}{R_1} \text{ and } \frac{Q_4}{R_4} = \frac{Q_2}{R_2}. \tag{20}$$

The expression of the stiffness coefficients is found by using the preceding 10 relations as

$$N = \mu_b, \tag{21a}$$

$$\begin{aligned} A = (1-\phi)K_s - \frac{2}{3}N - \frac{\beta\phi_1(1-\phi-K_b/K_s)K_s^2/K_f^{(1)}}{\beta(1-\phi-K_b/K_s)+K_s/K_f^{(1)}[\beta(\phi_1+\phi_3)+\phi_2+\phi_4]} \\ - \frac{\phi_2(1-\phi-K_b/K_s)K_s^2/K_f^{(1)}}{(1-\phi-K_b/K_s)+K_s/K_f^{(1)}[\beta(\phi_1+\phi_3)+\phi_2+\phi_4]} \\ - \frac{\beta\phi_3(1-\phi-K_b/K_s)K_s^2/K_f^{(2)}}{\beta(1-\phi-K_b/K_s)+K_s/K_f^{(2)}[\beta(\phi_1+\phi_3)+\phi_2+\phi_4]} \\ - \frac{\phi_4(1-\phi-K_b/K_s)K_s^2/K_f^{(2)}}{(1-\phi-K_b/K_s)+K_s/K_f^{(2)}[\beta(\phi_1+\phi_3)+\phi_2+\phi_4]}, \end{aligned} \tag{21b}$$

$$Q_1 = \frac{\beta(1-\phi-K_b/K_s)\phi_1 K_s}{\beta(1-\phi-K_b/K_s)+K_s/K_f^{(1)}[\beta(\phi_1+\phi_3)+\phi_2+\phi_4]}, \tag{21c}$$

$$Q_2 = \frac{(1-\phi-K_b/K_s)\phi_2 K_s}{(1-\phi-K_b/K_s)+K_s/K_f^{(1)}[\beta(\phi_1+\phi_3)+\phi_2+\phi_4]}, \tag{21d}$$

$$Q_3 = \frac{\beta(1-\phi-K_b/K_s)\phi_3 K_s}{\beta(1-\phi-K_b/K_s)+K_s/K_f^{(2)}[\beta(\phi_1+\phi_3)+\phi_2+\phi_4]}, \tag{21e}$$

$$Q_4 = \frac{(1-\phi-K_b/K_s)\phi_4 K_s}{(1-\phi-K_b/K_s)+K_s/K_f^{(2)}[\beta(\phi_1+\phi_3)+\phi_2+\phi_4]}, \tag{21f}$$

$$R_1 = \frac{[\beta(\phi_1+\phi_3)+\phi_2+\phi_4]\phi_1 K_s}{\beta(1-\phi-K_b/K_s)+K_s/K_f^{(1)}[\beta(\phi_1+\phi_3)+\phi_2+\phi_4]}, \tag{21g}$$

$$R_2 = \frac{[\beta(\phi_1+\phi_3)+\phi_2+\phi_4]\phi_2 K_s}{(1-\phi-K_b/K_s)+K_s/K_f^{(1)}[\beta(\phi_1+\phi_3)+\phi_2+\phi_4]}, \tag{21h}$$

$$R_3 = \frac{[\beta(\phi_1+\phi_3)+\phi_2+\phi_4]\phi_3 K_s}{\beta(1-\phi-K_b/K_s)+K_s/K_f^{(2)}[\beta(\phi_1+\phi_3)+\phi_2+\phi_4]}, \text{ and} \tag{21i}$$

$$R_4 = \frac{[\beta(\phi_1+\phi_3)+\phi_2+\phi_4]\phi_4 K_s}{(1-\phi-K_b/K_s)+K_s/K_f^{(2)}[\beta(\phi_1+\phi_3)+\phi_2+\phi_4]}. \tag{21j}$$

2.3. Plane-Wave Analysis and Solutions

By substituting the plane-wave kernel $e^{i(\omega t - \mathbf{k}\cdot\mathbf{x})}$ (where ω is the angular frequency, $\mathbf{k}$ is the wave number vector, and $\mathbf{x}$ is the spatial variable vector) into equations (12a)–(12h), the five-degree equation for *P* waves and one solution for *S* waves are obtained (the *S* wave solution only incorporates the Biot dispersion, see discussions in *Ba et al.* [2011]). The equation for the *P* waves is as follows:

$$\begin{vmatrix} a_{11}k^2+b_{11} & a_{12}k^2+b_{12} & a_{13}k^2+b_{13} & a_{14}k^2+b_{14} & a_{15}k^2+b_{15} \\ a_{21}k^2+b_{21} & a_{22}k^2+b_{22} & a_{23}k^2+b_{23} & a_{24}k^2+b_{24} & a_{25}k^2+b_{25} \\ a_{31}k^2+b_{31} & a_{32}k^2+b_{32} & a_{33}k^2+b_{33} & a_{34}k^2+b_{34} & a_{35}k^2+b_{35} \\ a_{41}k^2+b_{41} & a_{42}k^2+b_{42} & a_{43}k^2+b_{43} & a_{44}k^2+b_{44} & a_{45}k^2+b_{45} \\ a_{51}k^2+b_{51} & a_{52}k^2+b_{52} & a_{53}k^2+b_{53} & a_{54}k^2+b_{54} & a_{55}k^2+b_{55} \end{vmatrix} = 0, \tag{22}$$

and

$$\begin{aligned} a_{11} &= A + 2N + (\phi_2 Q_1 - \phi_1 Q_2)M_0^{(12)} + (\phi_3 Q_1 - \phi_1 Q_3)M_0^{(13)} + (\phi_4 Q_2 - \phi_2 Q_4)M_0^{(24)}, \\ a_{12} &= Q_1 + (\phi_2 Q_1 - \phi_1 Q_2)M_1^{(12)} + (\phi_3 Q_1 - \phi_1 Q_3)M_1^{(13)} + (\phi_4 Q_2 - \phi_2 Q_4)M_1^{(24)}, \\ a_{13} &= Q_2 + (\phi_2 Q_1 - \phi_1 Q_2)M_2^{(12)} + (\phi_3 Q_1 - \phi_1 Q_3)M_2^{(13)} + (\phi_4 Q_2 - \phi_2 Q_4)M_2^{(24)}, \\ a_{14} &= Q_3 + (\phi_2 Q_1 - \phi_1 Q_2)M_3^{(12)} + (\phi_3 Q_1 - \phi_1 Q_3)M_3^{(13)} + (\phi_4 Q_2 - \phi_2 Q_4)M_3^{(24)}, \\ a_{15} &= Q_4 + (\phi_2 Q_1 - \phi_1 Q_2)M_4^{(12)} + (\phi_3 Q_1 - \phi_1 Q_3)M_4^{(13)} + (\phi_4 Q_2 - \phi_2 Q_4)M_4^{(24)}, \end{aligned}$$

$$a_{21} = Q_1 + \phi_2 R_1 M_0^{(12)} + \phi_3 R_1 M_0^{(13)},\ \ a_{22} = R_1 + \phi_2 R_1 M_1^{(12)} + \phi_3 R_1 M_1^{(13)},$$
$$a_{23} = \phi_2 R_1 M_2^{(12)} + \phi_3 R_1 M_2^{(13)},\ \ a_{24} = \phi_2 R_1 M_3^{(12)} + \phi_3 R_1 M_3^{(13)},\ \ a_{25} = \phi_2 R_1 M_4^{(12)} + \phi_3 R_1 M_4^{(13)},$$
$$a_{31} = Q_2 - \phi_1 R_2 M_0^{(12)} + \phi_4 R_2 M_0^{(24)},\ \ a_{32} = -\phi_1 R_2 M_1^{(12)} + \phi_4 R_2 M_1^{(24)},$$
$$a_{33} = R_2 - \phi_1 R_2 M_2^{(12)} + \phi_4 R_2 M_2^{(24)},\ \ a_{34} = -\phi_1 R_2 M_3^{(12)} + \phi_4 R_2 M_3^{(24)},$$
$$a_{35} = -\phi_1 R_2 M_4^{(12)} + \phi_4 R_2 M_4^{(24)},\ \ a_{41} = Q_3 - \phi_1 R_3 M_0^{(13)},\ \ a_{42} = -\phi_1 R_3 M_1^{(13)},\ \ a_{43} = -\phi_1 R_3 M_2^{(13)},$$
$$a_{44} = R_3 - \phi_1 R_3 M_3^{(13)},\ \ a_{45} = -\phi_1 R_3 M_4^{(13)},\ \ a_{51} = Q_4 - \phi_2 R_4 M_0^{(24)},\ \ a_{52} = -\phi_2 R_4 M_1^{(24)},$$
$$a_{53} = -\phi_2 R_4 M_2^{(24)},\ \ a_{54} = -\phi_2 R_4 M_3^{(24)},\ \ a_{55} = R_4 - \phi_2 R_4 M_4^{(24)},$$
$$b_{11} = -\rho_{00}\omega^2 + i\omega(b_1 + b_2 + b_3 + b_4),\ \ b_{12} = -\rho_{01}\omega^2 - i\omega b_1,\ \ b_{13} = -\rho_{02}\omega^2 - i\omega b_2,$$
$$b_{14} = -\rho_{03}\omega^2 - i\omega b_3,\ \ b_{15} = -\rho_{04}\omega^2 - i\omega b_4,\ \ b_{21} = -\rho_{01}\omega^2 - i\omega b_1,\ \ b_{22} = -\rho_{11}\omega^2 + i\omega b_1,$$
$$b_{23} = b_{24} = b_{25} = 0,\ \ b_{31} = -\rho_{02}\omega^2 - i\omega b_2,\ \ b_{33} = -\rho_{22}\omega^2 + i\omega b_2,\ \ b_{32} = b_{34} = b_{35} = 0,$$
$$b_{41} = -\rho_{03}\omega^2 - i\omega b_3,\ \ b_{44} = -\rho_{33}\omega^2 + i\omega b_3,\ \ b_{42} = b_{43} = b_{45} = 0,\ \ b_{51} = -\rho_{04}\omega^2 - i\omega b_4,$$
$$b_{55} = -\rho_{44}\omega^2 + i\omega b_4,\ \text{ and } b_{52} = b_{53} = b_{54} = 0,$$

where

$$S_{12} = -\frac{\rho_f^{(1)}\omega^2 R_{12}^2 \phi_1^2 \phi_2^2 \phi_{20}}{3\phi_{10}(\phi_2 + \phi_4)} + \frac{\eta_f^{(1)} \phi_1^2 \phi_2^2 \phi_{20} R_{12}^2 i\omega}{3(\phi_2 + \phi_4)\kappa_1} - \phi_2^2 R_1 - \phi_1^2 R_2,$$
$$S_{13} = -\frac{\rho_f^{(1)}\omega^2 R_{13}^2 \phi_1^2 \phi_3}{3} + \frac{\eta_f^{(1)} \phi_1^2 \phi_3 \phi_{10} R_{13}^2 i\omega}{3\kappa_1} - \phi_3^2 R_1 - \phi_1^2 R_3,$$
$$S_{24} = -\frac{\rho_f^{(1)}\omega^2 R_{24}^2 \phi_2^2 \phi_4}{3} + \frac{\eta_f^{(1)} \phi_2^2 \phi_4 \phi_{20} R_{24}^2 i\omega}{3\kappa_2} - \phi_4^2 R_2 - \phi_2^2 R_4$$
$$M_0^{(12)} = \frac{(\phi_2 Q_1 - \phi_1 Q_2)/S_{12} + \phi_2 \phi_3 R_1 (\phi_3 Q_1 - \phi_1 Q_3)/(S_{12} S_{13}) - \phi_1 \phi_4 R_2 (\phi_4 Q_2 - \phi_2 Q_4)/(S_{12} S_{24})}{1 - (\phi_2 \phi_3 R_1)^2/(S_{12} S_{13}) - (\phi_1 \phi_4 R_2)^2/(S_{12} S_{24})},$$
$$M_1^{(12)} = \frac{\phi_2 R_1/S_{12} + \phi_2 (\phi_3 R_1)^2/(S_{12} S_{13})}{1 - (\phi_2 \phi_3 R_1)^2/(S_{12} S_{13}) - (\phi_1 \phi_4 R_2)^2/(S_{12} S_{24})},$$
$$M_2^{(12)} = \frac{-\phi_1 R_2/S_{12} - \phi_1 (\phi_4 R_2)^2/(S_{12} S_{24})}{1 - (\phi_2 \phi_3 R_1)^2/(S_{12} S_{13}) - (\phi_1 \phi_4 R_2)^2/(S_{12} S_{24})},$$
$$M_3^{(12)} = \frac{-\phi_1 \phi_2 \phi_3 R_1 R_3/(S_{12} S_{13})}{1 - (\phi_2 \phi_3 R_1)^2/(S_{12} S_{13}) - (\phi_1 \phi_4 R_2)^2/(S_{12} S_{24})},$$
$$M_4^{(12)} = \frac{\phi_1 \phi_2 \phi_4 R_2 R_4/(S_{12} S_{24})}{1 - (\phi_2 \phi_3 R_1)^2/(S_{12} S_{13}) - (\phi_1 \phi_4 R_2)^2/(S_{12} S_{24})},$$
$$M_0^{(13)} = \left(M_0^{(12)} \phi_2 \phi_3 R_1 + \phi_3 Q_1 - \phi_1 Q_3\right)/S_{13},$$
$$M_1^{(13)} = \left(M_1^{(12)} \phi_2 \phi_3 R_1 + \phi_3 R_1\right)/S_{13},$$
$$M_2^{(13)} = \left(M_2^{(12)} \phi_2 \phi_3 R_1\right)/S_{13},$$
$$M_3^{(13)} = \left(M_3^{(12)} \phi_2 \phi_3 R_1 - \phi_1 R_3\right)/S_{13},$$
$$M_4^{(13)} = \left(M_4^{(12)} \phi_2 \phi_3 R_1\right)/S_{13},$$
$$M_0^{(24)} = \left(-M_0^{(12)} \phi_1 \phi_4 R_2 + \phi_4 Q_2 - \phi_2 Q_4\right)/S_{24},$$
$$M_1^{(24)} = \left(-M_1^{(12)} \phi_1 \phi_4 R_2\right)/S_{24},$$
$$M_2^{(24)} = \left(-M_2^{(12)} \phi_1 \phi_4 R_2 + \phi_4 R_2\right)/S_{24},$$

$$M_3^{(24)} = \left(-M_3^{(12)}\phi_1\phi_4 R_2\right)/S_{24}, \text{ and}$$

$$\text{and } M_4^{(24)} = \left(-M_4^{(12)}\phi_1\phi_4 R_2 - \phi_2 R_4\right)/S_{24}.$$

The five roots correspond to a fast *P* wave (the classical compressional wave, denoted here by *P*1) and four slow Biot *P* waves denoted by *P*2, *P*3, *P*4, and *P*5.

The phase velocity is determined from the complex wave velocity $v = \omega/k$ and complex wave number k as [*Biot*, 1956; *Carcione*, 2014]

$$v_p = \frac{\omega}{Re(k)}, \tag{23}$$

The quality factor of the *P* waves is as follows:

$$Q = \frac{Re(k)}{2Im(k)}. \tag{24}$$

2.4. *P* Wave Modulus of Type-III Anelasticity With an Arbitrary Geometry of Fluid Distribution

Equations (23) and (24) give the compressional wave velocity and attenuation in a rock with Type-III anelasticity on the basis of the known geometry of fluid distribution: the host fluid, the inclusion fluid, and the fluid pocket radii. In real heterogeneous rocks partially saturated with two immiscible fluids, it is difficult to determine what fluid should be treated as the host one (actually, the fluid distribution pattern can change with the saturation procedures) [see *Cadoret et al*., 1995], especially for those in the moderate saturation range (30%–70%). In this range, each of the two fluids may become the host, and different zones of the same rock may have different host fluids.

For a rock saturated with fluid 1 (saturation S) and fluid 2 (saturation $1 - S$), an approximation can be made that in S of the rock volume fluid 1 is the host fluid, while in $1 - S$ of the rock volume fluid 2 is the host fluid. Moreover, the shear modulus N is not influenced by fluid saturation changes. Therefore, in order to give an estimate of wave velocity in the rock with an arbitrary geometry of fluid distribution, the Hill average is performed on the two *P* wave moduli, which are calculated by taking the different fluids as the host in equations (12a)–(12h) [*Toms et al*., 2006; *Ba et al*., 2016].

The modulus with fluid 1 as the host is

$$P_1 = Re\left(\frac{\omega^2\rho}{k_1^2}\right), \tag{25a}$$

and the modulus with fluid 2 as the host is

$$P_2 = Re\left(\frac{\omega^2\rho}{k_2^2}\right), \tag{25b}$$

where k_1 and k_2 are the complex wave numbers in the two cases, respectively. ρ is the rock density.

Then the Hill average is

$$\frac{1}{\overline{P}} = \frac{S}{P_1} + \frac{1-S}{P_2}, \tag{26}$$

where $\overline{P}$ is the *P* wave modulus of the partially saturated rock with arbitrary geometry, based on which compressional wave velocity can be calculated.

3. Examples

3.1. Muddy Siltstones With Submicroscopic Heterogeneity

In this first example, we consider the muddy siltstones, corresponding to rock samples collected from the tight oil reservoirs of the Qingshankou Formation (approximately 2 km depth) of northeast China. The samples have low porosity and low permeability. Intrapore clay with micropores is observed inside or connected to intergranular macropores, forming a submicroscopic double-porosity structure. The clay has high

compressibility in comparison with the main rock. WILFF (the so-called clay squirt flow) [*Best and McCann*, 1995] occurs at a scale smaller than the pore size.

When the muddy siltstones are partially saturated with water and gas (or oil), generally, those clay micropores are fully saturated with water because of the water wetability of clay and the effect of capillary forces. Gas or oil is mainly distributed inside the intergranular macropores, constituting microscopic gas pockets with water as the host fluid. The muddy siltstone saturated with two immiscible fluids is described with the DDP model here, where the two solid components are the intrapore clay (with micropores) and main skeleton (with intergranular macropores), with water as the host fluid and gas (oil) as the inclusion fluid. Clay is fully saturated with water (therefore, $S_2 = 0$) when the rock is partially saturated; then, we need not consider patchy saturation in the clay and phase 4 of equations (12a)–(12h) is neglected. However, for those intergranular pores, gas (oil) patches/pockets occurs.

Ultrasonic *P* and *S* wave velocities were measured for the five siltstone samples which are listed in Table 1 [*Ba et al*., 2016], at gas(nitrogen)-water partial saturation state and oil(kerosene)-water partial saturation state, respectively. Water saturation changes from 0 (full oil or gas saturation) to 100% (full water saturation) in the experiments. We used the experimental setup of *Guo et al*. [2009], *Zhou et al*. [2012], and *Hao et al*. [2016] at in situ conditions (confining pressure 50 MPa, pore pressure 25 MPa, and temperature 80°C). The experimental procedures are reported in *Ba et al*. [2016].

Sample *K* is selected as an example in the numerical modeling of wave anelasticity in muddy siltstones. The basic rock properties are given in Table 1. The bulk and shear moduli of the rock frame are determined according to the measured wave velocities at full gas saturation as 21.2 GPa and 12.1 GPa, respectively. The clay bulk modulus is taken as 1.3 GPa, while the mineral mixture density is 2.62 g/cm^3. The grain modulus K_s is reasonably estimated with a Hashin-Shtrikman bound [*Hashin and Shtrikman*, 1963] by assuming feldspar to be the host mineral. The intrapore clay with porosity $\phi_{20} = 0.02$ (based on the core analysis on pure mud rocks from the target formation, it shows the clay porosity ranges from 0.01 to 0.03, and the average is used in theoretical modeling) is assumed spherical with radius $R_{12} = 26$ μm (according to the clay/pore size from scanning electron microscopy analysis). The radius of the gas/oil pocket in the host frame is $R_{13} = 10$ μm. This radius can hardly be measured by any existing experimental technique for the sample undergoing experiments. *Lopes et al*. [2014] designed a setup with X-ray computerized tomography and active ultrasonic measurements; however, the resolution for the observed pockets is low. We consider it less than half of the size of the small siltstone pores. The gas/oil saturation S_1 in the host frame is taken as 0.87/0.85 according to the measurements in the partial saturation experiments. The clay content of the whole rock is $v_{\text{clay}} = 5.5\%$, and the volume ratio of the intrapore clay is then approximately determined as $v_2 = \phi v_{\text{clay}}$; therefore, the four porosities are, respectively, $\phi_1 = v_1\phi_{10}(1 - S_1)$, $\phi_2 = v_2\phi_{20}$, $\phi_3 = v_1\phi_{10}S_1$, and $\phi_4 = 0$. The density, moduli, and viscosity of in situ nitrogen, kerosene, and water are 0.3 g/cm^3, 0.089 GPa, and 0.031 cP, 0.79 g/cm^3, 1.27 GPa, and 2.1 cP, and 0.98 g/cm^3, 2.53 GPa, and 0.35 cP, respectively (at temperature 80°C and pore pressure 25 MPa).

By using equations (12a)–(12h) and equations (23) and (24), Figure 1 gives the compressional wave velocity and attenuation as a function of the frequency, corresponding to sample *K*. The ultrasonic wave velocities at full gas, oil, and water saturations and the two partial saturations are also given. The velocity dispersion and attenuation of compressional waves mainly occur in the ultrasonic band (10^4–10^7 Hz). Regarding the curves at full saturation, the DDP model reduces to the original BR model of double porosity (DP), where the attenuation peak and the dispersion inflection point move to the low frequencies with higher fluid viscosity (similar results on the DP model of clay squirt flow in the fully saturated siltstones have been given in *Ba et al*. [2016]). The single attenuation peak on each curve of the three full saturations is caused by fabric heterogeneity. The curve for full oil saturation gives the highest peak attenuation, and that of full gas saturation gives the lowest.

For the two curves at partial saturation (13% gas and 87% water and 15% oil and 85% water) in Figure 1, water is considered to be the host fluid in the intergranular macropores (the host skeleton) and clay is assumed fully water saturated. The coupling effect between Type-I anelasticity (clay squirt flow of intrapore clay) and Type-II anelasticity (patchy saturation of intergranular pores) causes two associated attenuation peaks at the ultrasonic frequencies. For the gas-water saturation case, the two peaks tend to merge, and the highest peak is controlled by Type-III anelasticity, the overlapping effect of fabric heterogeneity and patchy saturation. For the oil-water saturation case, they completely merge. The bandwidth of the main wave

Table 1. Tight Oil Siltstone Properties [*Ba et al.*, 2016]

Samples	Porosity (%)	Permeability (md)	Dry Density (g/cm^3)	Clay (%)	K_b (GPa)	μ_b (GPa)	Clay Bulk Modulus (g/cm^3)	Clay Radius R_{12} (μm)	Host Pocket Radius R_{13} (μm)
H	6.45	0.097	2.38	5.5	30.5	16	0.7	30	10
I	10.87	0.39	2.29	5.5	21.6	12.6	1.1	72	45
J	12.75	0.17	2.3	4.4	22.2	13.5	0.5	36	5
K	13.09	0.08	2.28	5.5	21.2	12.1	1.3	26	10
L	13.97	0.084	2.26	5.5	20	11.8	0.6	30	10

dispersion/attenuation of WILFF is broadened at partial saturation states in comparison with those of the full saturation. The dispersion inflection points and the attenuation peaks on the curve of oil and water partial saturation occur at lower frequencies than those of gas and water saturation. The highest attenuation peak for oil and water partial saturation is lower than that of full oil saturation, while the highest attenuation peak of gas and water partial saturation is higher than that of full gas (or full water) saturation. The attenuation curve of oil and water saturation is very close to that of full water saturation. In Figure 1a (all the five cases), the predictions (based on the given rock/fluid parameters) agree well with the laboratory data at the ultrasonic frequency.

Since the intrapore clay is assumed fully saturated with water, only three types of pores are considered in equations (12a)–(12h), yielding one fast and three slow compressional waves. Figures 2–4 show the three slow compressional wave velocity and attenuation curves (*P*2, *P*3, and *P*4) as a function of frequency for the muddy siltstones. For the three full saturation states, the DDP model reduces to the DP model and there is no inclusion fluid; therefore, only two slow waves (*P*2 and *P*3) are given. All the three slow waves are diffusive modes [*Biot*, 1956]. *P*2 (Figure 2) is caused by the motion of sloshing effect between the host fluid in the host skeleton and the solid (the inclusion fluid is neglected at full saturation), while *P*3 (Figure 3) corresponds to the host fluid in the inclusion skeleton and the solid, and *P*4 (Figure 4) to the inclusion fluid in the host

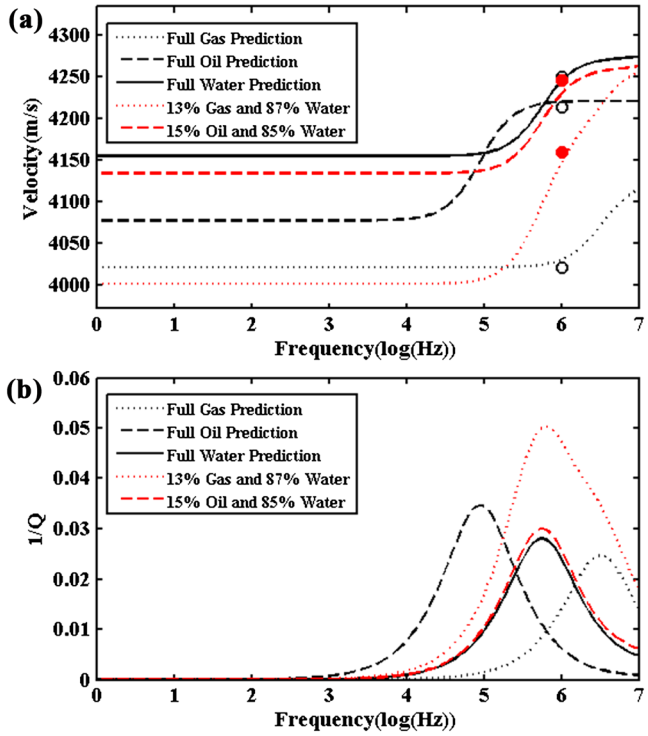

Figure 1. Fast compressional-wave (*P*1) (a) velocity and (b) attenuation as a function of frequency corresponding to the DDP model of the fluid-saturated siltstone (sample *K*). Ultrasonic measurement data of compressional-wave velocity of sample *K* (data are from *Ba et al.* [2016]) are comparatively given in Figure 1a, where the black open circles and the red filled circles correspond to data at full saturation and partial saturation, respectively.

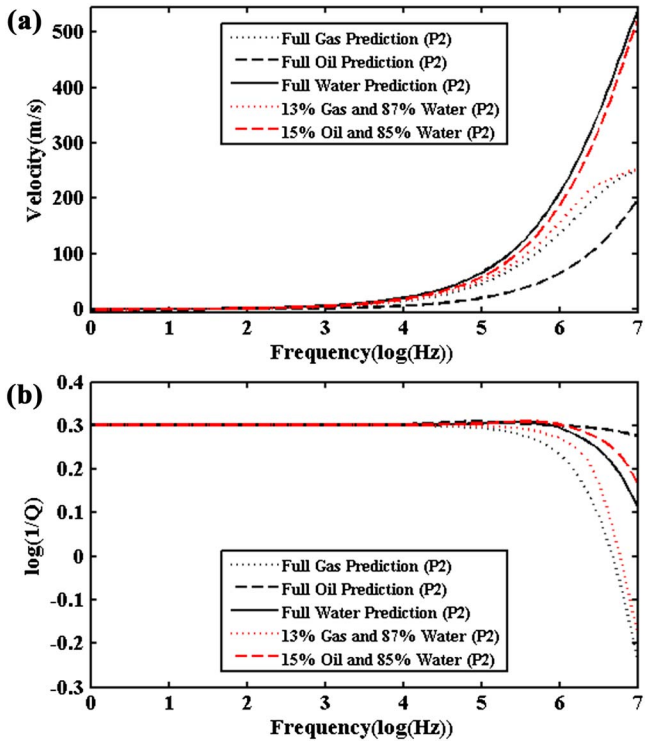

Figure 2. Phase (a) velocity and (b) attenuation of the Biot slow *P* wave *P*2 as a function of frequency corresponding to the DDP model of the fluid-saturated siltstone (sample *K*).

skeleton. For the slow waves, 1/*Q* decreases with frequency. Extremely high dissipation can be observed on the *P*3 and *P*4 curves, which can hardly be experimentally observed, even at ultrasonic frequencies.

In Figures 2 and 3, each velocity (attenuation) curve of the *P*2 and *P*3 modes at oil and water partial saturation is located between the corresponding full oil and full water curves, while the same happens for gas. In Figure 3, the *P*3 velocity and attenuation curves at the two partial saturation states almost concur with those of the full water saturation state. In Figure 4, the *P*4 velocity of oil-water saturation is higher than that of gas-water saturation, due to the fluid property differences between oil (kerosene) and gas (nitrogen).

Theoretical predictions of compressional wave velocity of the DDP model for the five muddy siltstones listed in Table 1 are given in Figures 6 and 7, compared to the experimentally measured compressional wave velocities at partial saturations (for gas-water and oil-water). The Hill average (equation (26)) is used for estimating the wave velocities at partial saturation states with arbitrary geometry, since we can hardly determine which fluid should be treated as the host fluid. *Ba et al*. [2016] have shown that the Biot-Gassmann-Hill (BGH) bound [*Gassmann*, 1951; *Biot*, 1956; *Toms et al*., 2006] provides good estimations of compressional wave velocity in the partially saturated siltstones in the range of water saturation of 0–60%, where the rock is relaxed from clay squirt flow mechanism. However, the BGH bound is also shown to be invalid for the rock at partial oil-water saturation and at high water saturations of the case of partial gas-water saturation, where the solid skeleton is stiffened by unrelaxation of Type-I anelasticity. A Biot-Rayleigh-Hill bound was then presented by *Ba et al*. [2016] to predict wave velocity at the stiffened states. However, this approach cannot simultaneously work for the rocks at the unrelaxed states. It is apparently shown in Figure 1a that sample *K* at full gas saturation is mostly relaxed, contrary to the case of full liquid saturation, and the DDP model provides reasonable predictions of the wave velocities for all the five different saturation conditions. As shown in Figure 5 for samples *H*, *I*, and *J* and Figure 6 for samples *K* and *L*, the predictions from the DDP model show a good agreement with the experimental data, both for oil-water and gas-water saturations. Note that a unique set of rock parameters is used here for the modeling in each sample, given in Table 1.

3.2. Low-Porosity Dolomites With Microscopic Heterogeneity

In the second example, we consider a series of low-porosity dolomite specimens, as listed in Table 2. The five samples (DT1–5) were collected from the Cambrian formations, Tarim Basin, northwest China. Rocks from this formation are composed of almost pure dolomite, which are light grey reef dolomite and granular dolomite with dissolved pores. Other three dolomite samples (DS1–3) were collected from the Permian formations, Sichuan Basin, southwest China. These rocks are brown dolomites with intergranular dissolved pores and rare clay. The formations are more than 4 km depth.

Similarly to the first example, at partial saturation (with water and gas/oil) of the in situ carbonate rocks with microscopic grain cracks/contacts, generally soft cracks are fully saturated with water because of the control effect of capillary force. Gas or oil is distributed in the intergranular pores, constituting

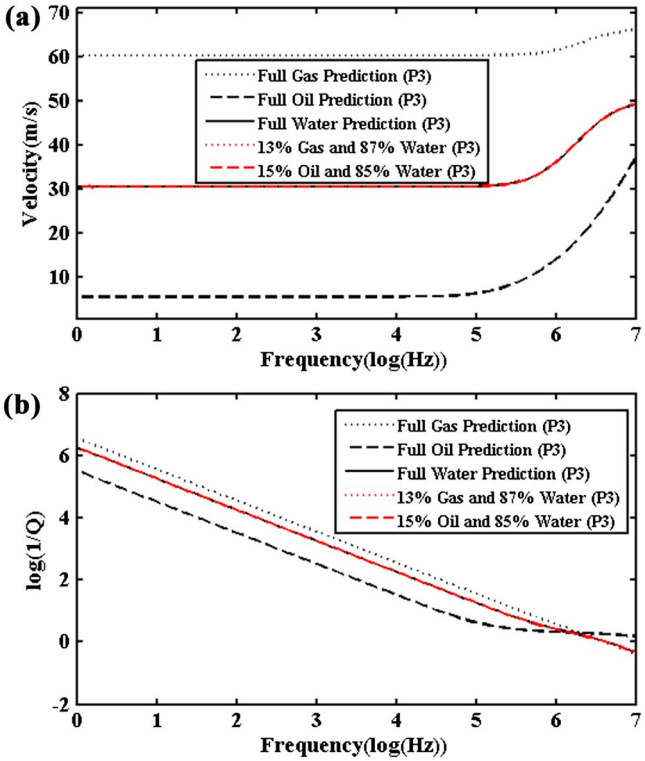

Figure 3. Phase (a) velocity and (b) attenuation of the Biot slow *P* wave *P*3 as a function of frequency corresponding to the DDP model of the fluid-saturated siltstone (sample *K*).

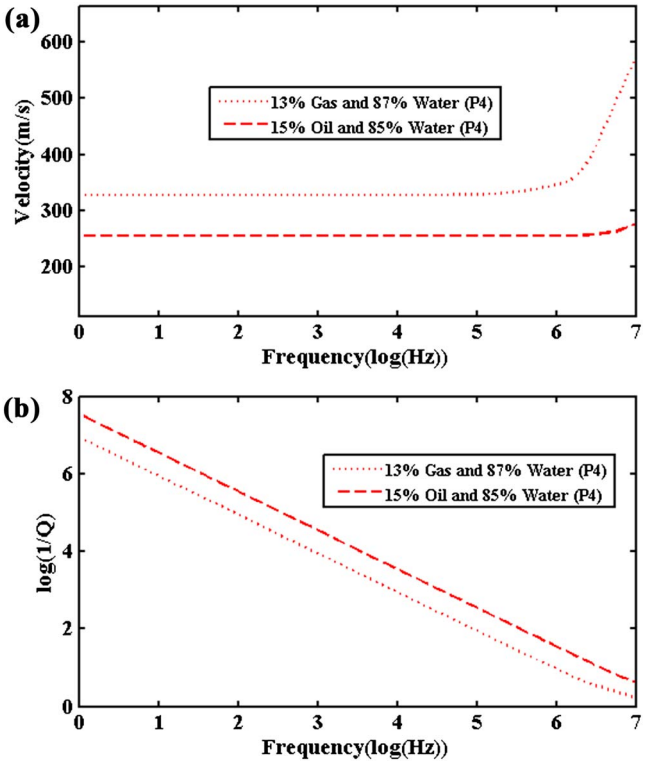

Figure 4. Phase (a) velocity and (b) attenuation of the Biot slow *P* wave *P*4 as a function of frequency corresponding to the DDP model of the fluid-saturated siltstone (sample *K*).

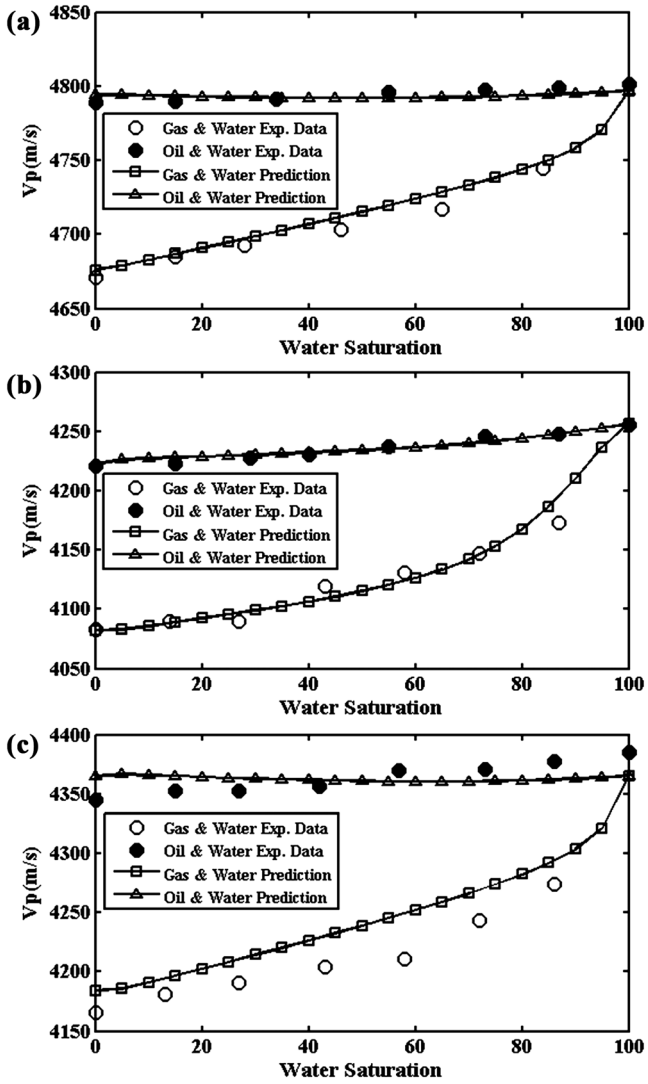

Figure 5. Comparisons between experimental data and the DDP model for compressional-wave velocity as a function of water saturation for the partially saturated tight siltstones: (a) sample *H*, (b) sample *I*, and (c) sample *J*. The experimental data are from *Ba et al*. [2016].

gas/oil pockets (in some rocks they can be larger than the pore/grain size) with water as the host fluid. In some cases, the pocket may have a mesoscopic size, which depends on the fabric texture (for instance, large pores resulting from dissolution in carbonates), fluid distribution, and saturation [*Lebedev et al*., 2009]. In a DDP model of partially saturated dolomite, the two components are the grain cracks/contacts (the size of them is approximately the diameter of the cross section of dolomite grains, 10–1000 μm) and the main porous solid skeleton. Crack/contact is fully saturated with water and phase 4 is neglected.

Ultrasonic wave velocities are measured for the eight dolomite samples which are listed in Table 2, at gas(nitrogen)-water and oil(kerosene)-water partial saturations and at confining pressure 80 MPa, pore pressure 10 MPa, and temperature 20°C. Water saturation changes from 0 to 100%. The same experimental setup and procedures are used as those of the first example.

Sample DS2 is selected as an example for the numerical results of clean low-porosity dolomite, where the basic properties are given in Table 2. The bulk and shear moduli of the dry rock are determined according to the measured velocities at full saturation states as 40.8 GPa and 26.2 GPa, respectively. The bulk modulus of the cracked grain or grain contact is taken as 8 GPa. The density of the mineral (pure dolomite) is 2.84 g/cm^3, and its grain modulus (K_s) is 95 GPa. We assume that $p = 2.4\,\%$ of the dolomite grains may contain flat

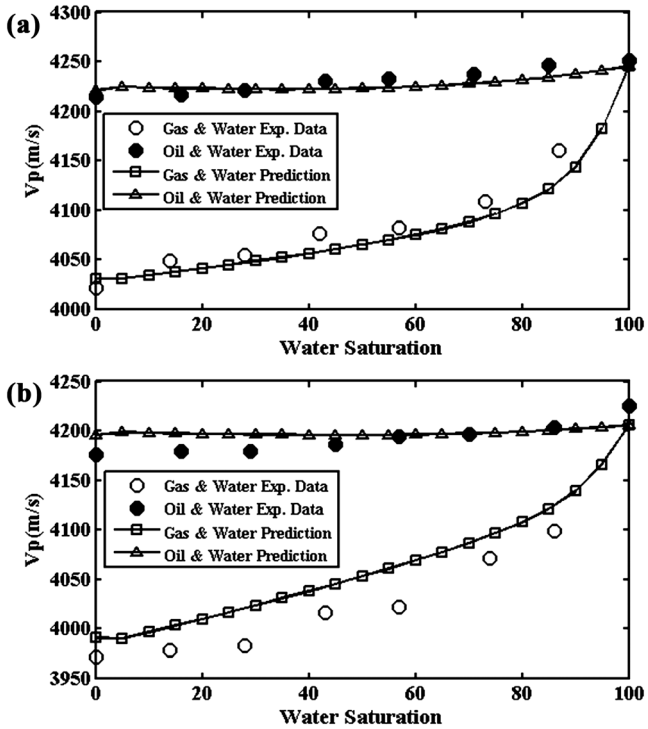

Figure 6. Comparisons between experimental data and the DDP model for compressional-wave velocity as a function of water saturation for the partially saturated tight siltstones: (a) Sample *K* and (b) sample *L*. The experimental data are from *Ba et al*. [2016].

cracks/contacts (Here p denotes the volume ratio of cracked grains to all grains. Grain contacts and cracks mainly occur in those large dolomite grains with a diameter larger than 140 μm, which can be stiff enough to sustain soft pores, and cracked-grain volume ratio is generally less than 5% in the carbonates from the two areas. It is taken around the average value and allows for an explanation of the observed dispersion), and the porosity of the grain contact is $\phi_{20} = 0.09$ (it is modeled in a similar way as *Pride et al*. [2004]: if the grain is modeled as a cylinder of axial length 140 μm, containing a transverse crack with an average effective aperture 10–15 μm, the average crack porosity of the grain is approximately 0.09) with a radius $R_{12} = 70$ μm (half the grain size). The radius of the gas/oil pocket in the host skeleton is $R_{13} = 11$ μm and $S_1 = 0.77$ (according to saturation measurements). The four porosities are $\phi_1 = (\phi - p(1-\phi)\phi_{20})S_1$, $\phi_2 = p(1-\phi)\phi_{20}$, $\phi_3 = (\phi - p(1-\phi)\phi_{20})(1-S_1)$, and $\phi_4 = 0$. The density, moduli, and viscosity of in situ gas (nitrogen), oil (kerosene), and water are 0.25 g/cm^3, 0.023 GPa, and 0.022 cP, 0.82 g/cm^3, 1.6 GPa, and 18 cP, and 1 g/cm^3, 2.24 GPa, and 0.98 cP, respectively (at a temperature of 20°C and pore pressure of 10 MPa).

Similar to the muddy siltstone example, *P*5 is neglected since the fourth phase of porosity is not considered, and only the *P*1 and *P*2 results are given for the three full saturation states. Figure 7 shows the compressional wave velocity and attenuation as a function of frequency for the DDP model of the clean dolomites, and

Table 2. Low-Porosity Dolomite Properties

Samples	DT1	DT2	DT3	DT4	DT5	DS1	DS2	DS3
Porosity (%)	5.10	5.34	5.47	12.08	12.28	11.63	11.73	11.75
Permeability (md)	0.091	0.458	0.174	162.753	22.819	0.661	0.138	0.075
Dry density (g/cm^3)	2.69	2.66	2.67	2.41	2.44	2.45	2.51	2.45
p (%)	3.2	2.8	1.9	3.4	3.0	2.9	2.4	3.0
K_b (GPa)	60.5	60.9	61.7	35.4	35.9	39.5	40.8	39.7
μ_b (GPa)	36.2	35.9	36.4	23.5	23.2	25.1	26.2	25.2
Contact modulus (GPa)	7	12	13	12	10	7	8	7
Contact radius R_{12} (μm)	50	90	55	800	350	145	70	55
Host pocket radius R_{13} (μm)	7	40	28	235	315	32	11	9

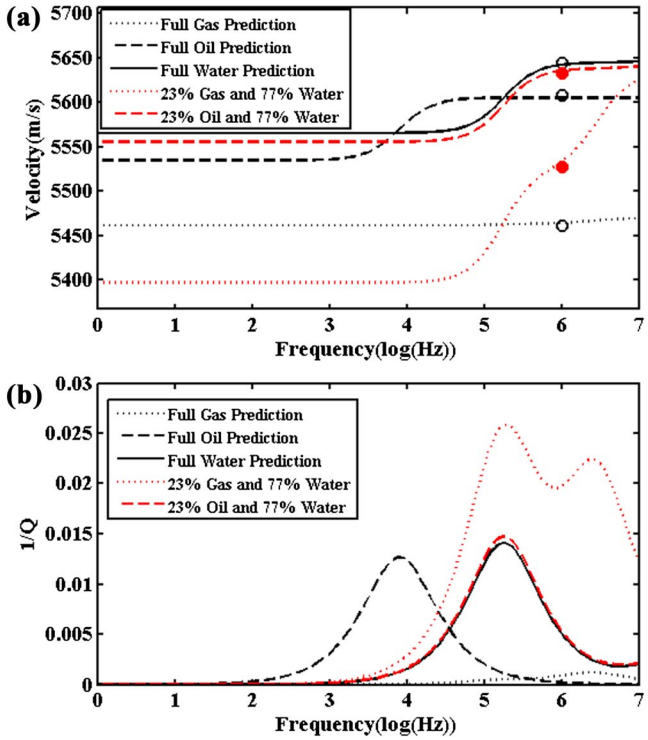

Figure 7. Fast compressional wave (*P*1) (a) velocity and (b) attenuation as a function of frequency corresponding to the DDP model of the fluid-saturated dolomite (sample DS2). Ultrasonic measurement data of compressional wave velocity in the sample DS2 are comparatively given in Figure 7a, where the black open circles and the red filled circles correspond to data at full saturation and partial saturation, respectively.

correspondingly, Figures 8–10 give the frequency-dependent slow compressional wave velocities and attenuation of *P*2, *P*3, and *P*4.

As is shown by Figure 7, fast compressional wave dispersion and attenuation mainly occurs in the frequency range of 10^3–10^7 Hz for the dolomites. The characteristic frequency band of anelasticity (see Figure 7) is slightly lower than that of the muddy siltstones (see Figure 1), which is due to the difference in heterogeneity scale: the intrapore clay of muddy siltstone is generally smaller than 50 μm, while the grain contact/microcrack in pure dolomites has a larger size, in the range 50–800 μm. The dolomite curves at full gas saturation give very weak dispersion and attenuation, because the gas modulus and density are very low at the pore pressure of 10 MPa, and the rock is nearly relaxed. The curves for full oil saturation exhibit the strongest dispersion/dissipation in the sonic band (10^3–10^4 Hz). For the gas and water partial saturation cases, the two inflection points of the velocity and the two attenuation peaks are quite obvious in Figures 7a and 7b (the attenuation peak or inflection point at $10^{5.3}$ Hz is mainly caused by fabric heterogeneity, and that at $10^{6.4}$ Hz is mainly caused by patchy saturation), while the model results of oil-water are close to those at full water saturation, where the two attenuation peaks merge. A comparison between Figures 7b and 1b shows that the model predicts higher attenuation in muddy siltstones than clean dolomites. As is shown by Figure 7a, the model predictions also agree well with the laboratory data at the ultrasonic frequency.

In Figures 7–10, *P*2 is due to the differential motion between the host fluid in the host skeleton and the solid part, while *P*3 and *P*4 correspond to the host fluid in the inclusion skeleton and inclusion fluid in the host skeleton. By comparing Figure 9 with Figure 3, the *P*3 wave velocity in the dolomite example is obviously higher than that in siltstone example. In Figure 9, the curve of gas-water partial saturation is totally different to the curves at the other states, due to the low density/modulus of gas at 10 MPa in comparison with oil or water. In Figure 10, the *P*4 velocity of the oil-water saturation is lower than that of the gas-water saturation.

Corresponding to the eight dolomites, the theoretical predictions of the DDP model with arbitrary geometries are given in Figures 11–13, in comparison with the experimental data at the partial saturation states. The squirt-flow mechanism (microscopic scale) caused by the grain contacts/cracks is considered here instead

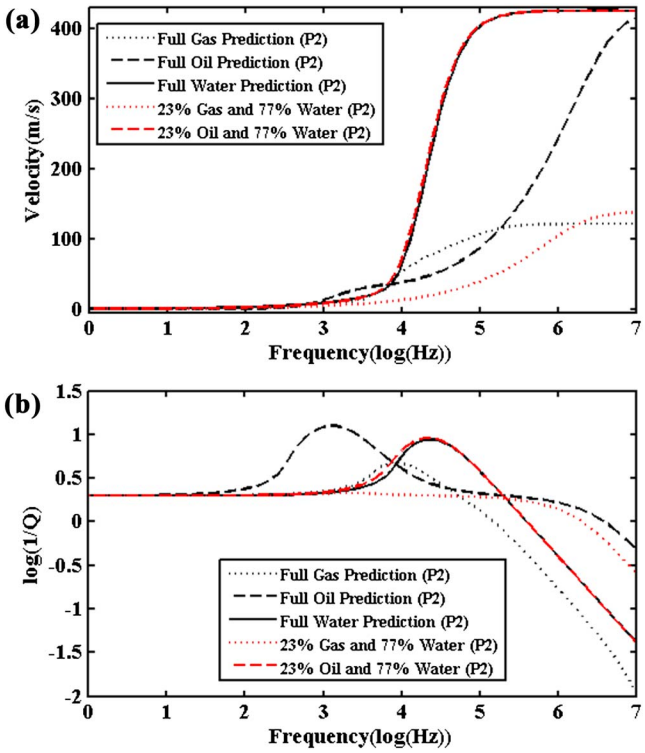

Figure 8. Phase (a) velocity and (b) attenuation of the Biot slow *P* wave *P2* as a function of frequency corresponding to the DDP model of the fluid-saturated dolomite (sample DS2).

of the clay squirt flow mechanism used in the first example (siltstones). The dolomite partially saturated with gas and water (at low pore pressure) is mostly relaxed, while the same rock saturated with oil and water mixture is unrelaxed. By using the single set of rock properties and coefficients listed in Table 2 for each sample, the results show that the DDP model provides a good description of the relationships between compressional wave velocity and fluid saturation in these partially saturated dolomites, for both the relaxed and unrelaxed/stiffened states.

3.3. Tight Gas Sandstones With Mesoscopic Heterogeneity

In the third example we consider a tight sandstone sample (sample TS: porosity 0.15, dry-rock density 2.25 g/cm^3, and permeability 1 mD) collected from the Triassic formation of a tight gas field, middle Sichuan Basin, southwest China. The formation is located at approximately

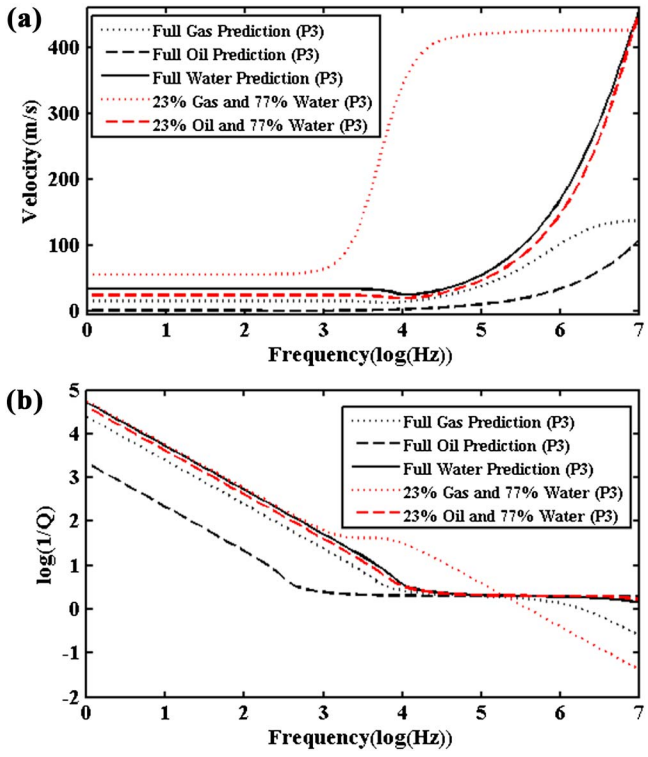

Figure 9. Phase (a) velocity and (b) attenuation of the Biot slow *P* wave *P3* as a function of frequency corresponding to the DDP model of the fluid-saturated dolomite (sample DS2).

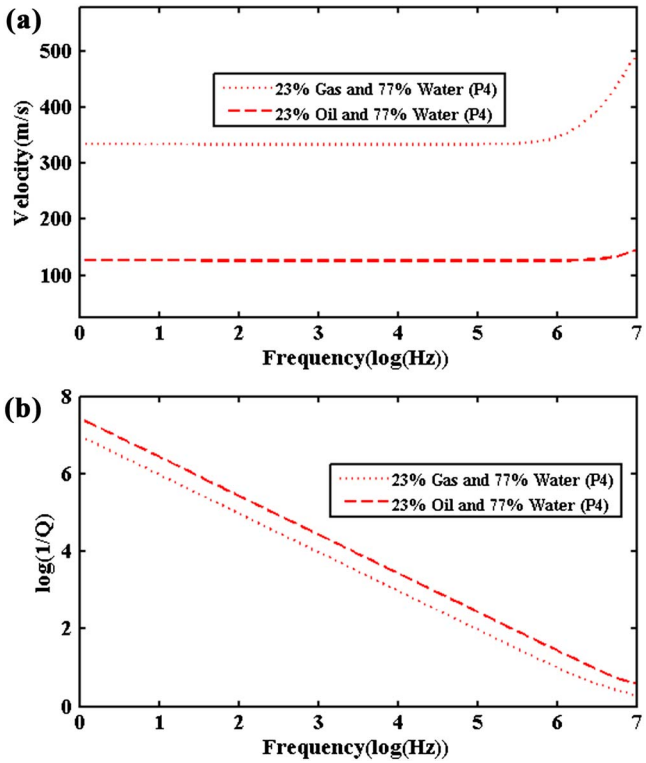

Figure 10. Phase (a) velocity and (b) attenuation of the Biot slow *P* wave *P*4 as a function of frequency corresponding to the DDP model of the fluid-saturated dolomite (sample DS2).

2 km depth. The sample is moderately sorted, and the minerals are mainly quartz and debris (with siltstones, clay, phyllite, feldspar, and mica fragments). The sample has low porosity and low permeability. Some less consolidated sands with higher porosity and permeability can be observed in the main rock skeleton of the tight sandstone.

Low-frequency measurement techniques [*Batzle et al*., 2006; *Adam et al*., 2006] are applied on the sample (cylinder 38.1 mm in diameter and 43 mm high) to measure the wave velocities at seismic frequencies (10^1–10^3 Hz) and temperature of 20°C, confining pressure of 14 MPa and pore pressure of 3.5 MPa. Measurements are performed at full air, butane, and water saturation. The stress strain approach by using axial deformation (for transducers) with resistive strain gauges bonded directly to the sample is utilized, where the bonded gauges are not sensitive to the equipment resonance. Strain due to a low-frequency sinusoidal stress (applied with a mechanical shaker) is measured. The rock bulk and shear moduli (then the wave velocities) are estimated from the strains on the rock and on an aluminum standard according to *Batzle et al*. [2006]. Two sets of measurements are performed on the sample with the two different sets of gauges.

A mesoscopic double-porosity structure is considered for the two components of the less consolidated sand (uncemented or loose-contact granular material) as the inclusions and well-consolidated tight sandstone as the host. The less consolidated sand is embedded in the main skeleton of the tight sandstone, and when the rock is partially saturated with light gas and water, more gas tends to migrate into the larger pores between the loose-contact grains and accumulates, resulting in larger gas pockets and high gas saturation in the local high-porosity and high-permeability zones, while smaller gas pockets are distributed in the host tight skeleton with a lower gas saturation.

The bulk and shear moduli of the dry rock are determined as 8.37 GPa and 8.22 GPa, respectively. The bulk modulus of the less consolidated sand is taken as 0.13 GPa, according to the properties of loose-contact granular material, which explains the observed strongest dispersion, and the density of the mineral mixture is 2.65 g/cm^3. The grain modulus of the mineral mixture K_s is 22 GPa. We assume that the sandstone contains $v_2 = 7.5$ % of less consolidated components (uncemented sand and debris) according to the mineral content

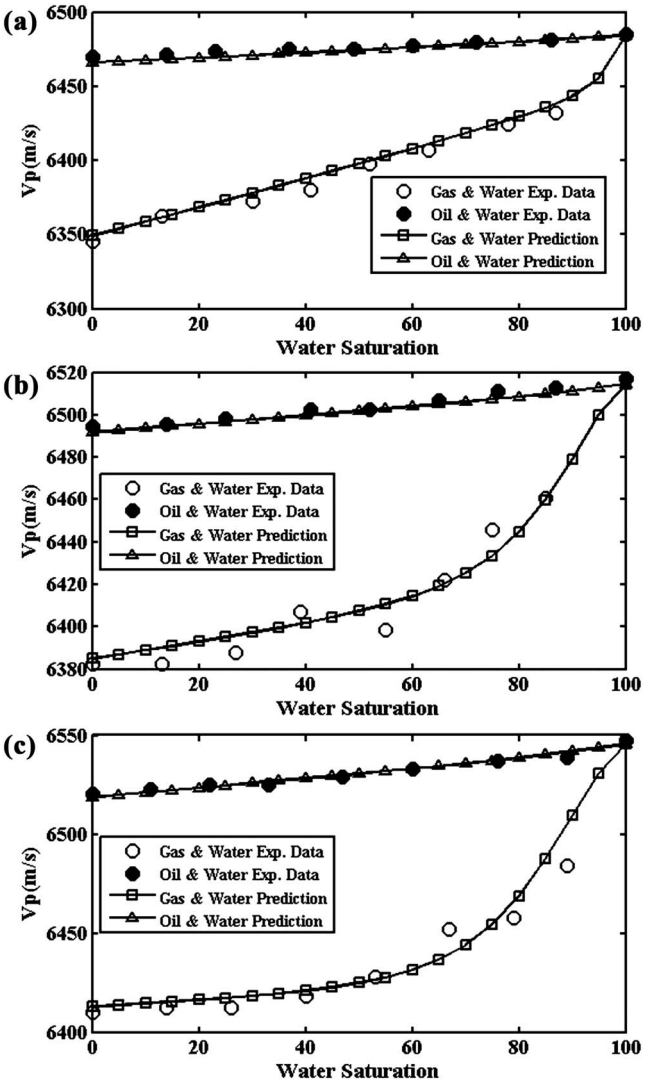

Figure 11. Comparisons between experimental data and the DDP models for compressional wave velocity as a function of water saturation for the partially saturated clean dolomites: (a) sample DT1, (b) sample DT2, and (c) sample DT3.

of the rock specimens from the target formation. The inclusion frame has a porosity $\phi_{20} = 0.25$, according to the properties of the less consolidated sand from the formation, and a radius $R_{12} = 4$ mm, which is larger than the grain size and allows for an explanation of the low-frequency dispersion. The host frame has a porosity $\phi_{10} = 0.142$. In the modeling, the radius of the gas pocket in the host frame is $R_{13} = 200\,\mu$m and $S_1 = 0.95$, and the radius of the gas pocket in the less consolidated sand is $R_{24} = 1$ mm and $S_2 = 0.7$. The four porosities are $\phi_1 = v_1 S_1 \phi_{10}$, $\phi_2 = v_2 S_2 \phi_{20}$, $\phi_3 = v_1(1 - S_1)\phi_{10}$, and $\phi_4 = v_2(1 - S_2)\phi_{20}$. The density, moduli, and viscosity of air, butane, and water are 0.07 g/cm^3, 0.0037 GPa, and 0.009 cP, 0.604 g/cm^3, 0.717 GPa, and 0.172 cP, and 1.033 g/cm^3, 2.45 GPa, and 1.1 cP (at a temperature of 20°C and pore pressure of 3.5 MPa).

Figure 14 shows the compressional wave velocity and attenuation as a function of frequency for the full and partially saturated tight sandstone. The experimental data of the low-frequency stress strain measurements at the three full saturation states show very strong *P* wave velocity dispersion and attenuation in the seismic band (10^1–10^3 Hz), where the theoretical model generally provides an appropriate agreement with the data, and based on that, the curves at partial saturation are also shown. The strong anelasticity in the seismic band is caused by the mesoscopic heterogeneity. The peak value of the attenuation curve at full water saturation is close to that of full butane saturation, and the attenuation/dispersion at full water saturation occurs at relatively lower frequencies than that at full butane saturation. Regarding the partial saturation curves, more than

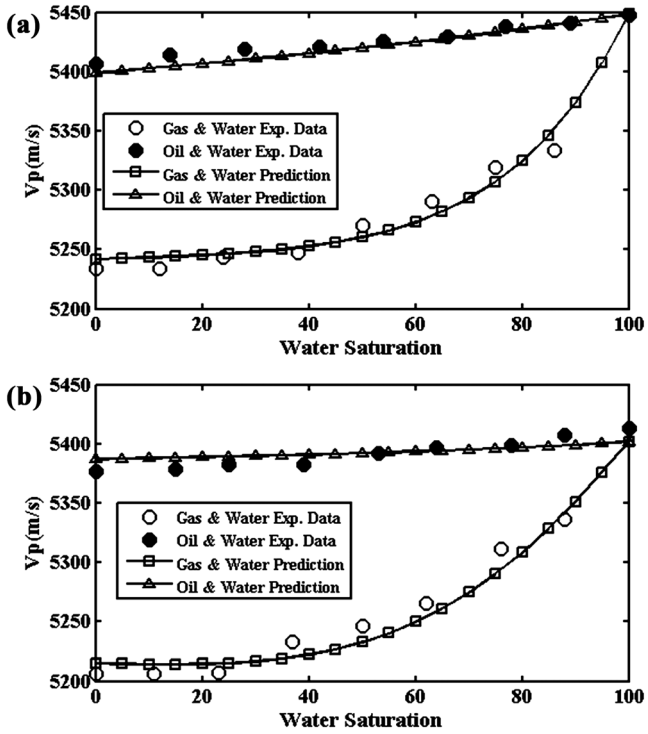

Figure 12. Comparisons between experimental data and the DDP models for compressional wave velocity as a function of water saturation for the partially saturated clean dolomites: (a) Sample DT4 and (b) sample DT5.

one attenuation peak are observed, and the characteristic frequency band of anelasticity by WILFF is broadened. In the case of air-water partial saturation, the peaks merge in a coupling effect, and the patchy saturation in the inclusion skeleton dominates the anelasticity features (with a $1/Q$ peak of 0.122, i.e., $Q = 8$), which strengthens the dissipation effect by a coupled WILFF, and causes the attenuation peak moving to the high frequencies in comparison with the full water saturation case. In the case of butane-water saturation, the attenuation peak at $10^{1.9}$ Hz is caused by the overlapping effect of fabric heterogeneity and patchy saturation in the host skeleton, and that at $10^{4.2}$ Hz is mainly caused by patchy saturation in the inclusion skeleton.

Figures 15–18 show the four slow compressional wave velocity and attenuation curves, where *P*2, *P*3, *P*4, and *P*5 are due to the effect between the host fluid in the host skeleton and solid, the effect between the host fluid in the inclusion skeleton and solid, the effect between the inclusion fluid in the host skeleton and solid, and the effect between the inclusion fluid in the inclusion skeleton and solid, respectively. All the slow waves are highly diffusive. For *P*4 and *P*5, the velocities of the butane-water partial saturation are higher than those of the air-water partial saturation.

3.4. Heterogeneity Scale and Frequency-Dependent Attenuation

Figure 19a shows the relationship between the rock-fabric heterogeneity and fluid-pocket heterogeneity scales for all the 14 specimens. The parameter related to fabric heterogeneity (the radius of the inclusion skeleton) is determined by theoretical modeling on the experimental data at full saturation. For siltstones and dolomites, the parameter of fluid heterogeneity (fluid pocket radius) is obtained by modeling on the experimental data at all the partial saturation regimes, while for the tight sandstone sample, the two fluid pocket sizes in the inclusion skeleton and the host skeleton, respectively, are based on the rock physics properties, since no low-frequency measurements were made on the sample at partial saturation. The results show that generally the fluid-heterogeneity scale is correlated to the rock fabric heterogeneity scale, and the fluid-pocket size increases with larger fabric-heterogeneity size. Siltstones show the smallest fabric inhomogeneity ($<$0.1 mm), carbonates show moderate values ($<$1 mm), and the sandstone shows a mesoscopic

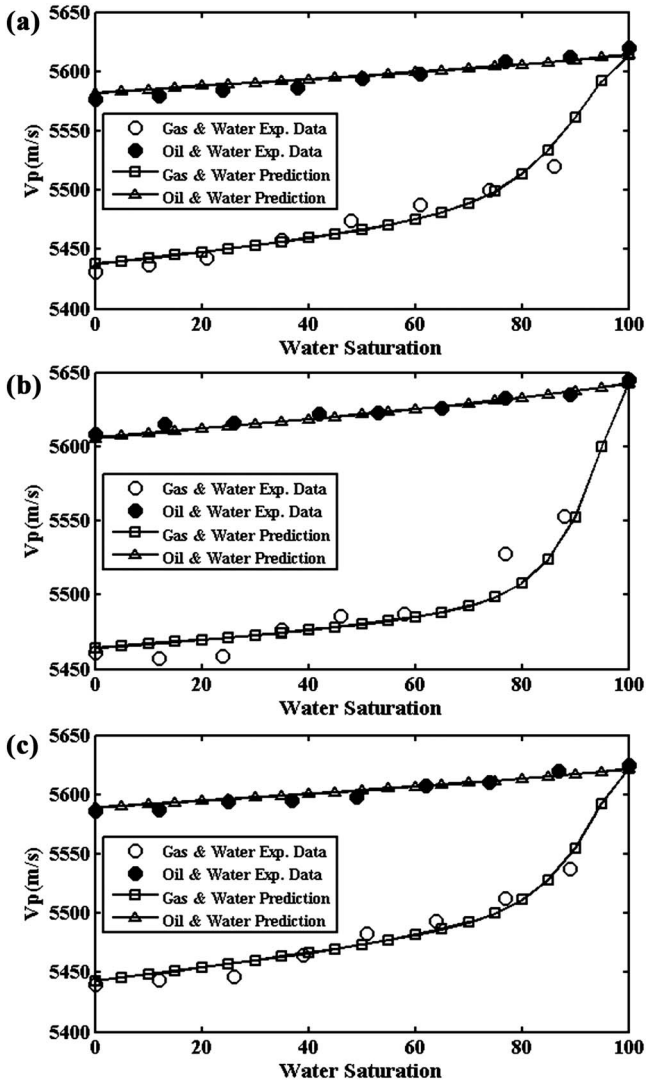

Figure 13. Comparisons between experimental data and the DDP models for compressional wave velocity as a function of water saturation for the partially saturated clean dolomites: (a) Sample DS1, (b) sample DS2, and (c) sample DS3.

heterogeneity of the order of millimeters. A larger fluid-pocket size is also found in dolomites compared to siltstones. For each sample of dolomite and siltstone, the highest peak attenuation is obtained based on the model results of all the partial saturation regimes (oil-water saturation and gas-water saturation) where measurements were made, and the highest peak generally occurs at high water saturations (water saturation $>$70%) of the gas-water partial saturation state. For the tight sandstone, the attenuation is given at 8% air and 92% water saturation (shown as the red dotted curve in Figure 14). The peak attenuation is not significant with fabric heterogeneity or fluid pocket sizes, and it should be more relevant with the compressibility contrast between different components [*Ba et al.*, 2015b]. The tight sandstone exhibits the largest anelasticity according to the example. Figure 19a also shows significant attenuation variations between the different dolomite samples (although all these samples are almost pure dolomite), which should be attributed to the strong variations of texture and cement of carbonates.

Figure 19b shows the highest peak attenuation of each sample as a function of frequency. The corresponding characteristic frequency of the peak attenuation is also given. It can be seen that the strongest anelasticity of the partially saturated dolomites and siltstones mainly occurs in the ultrasonic band ($>10^5$ Hz), while that of the partially saturated tight sandstone occurs in the sonic band. Apparently, it is related to the intrinsic fabric

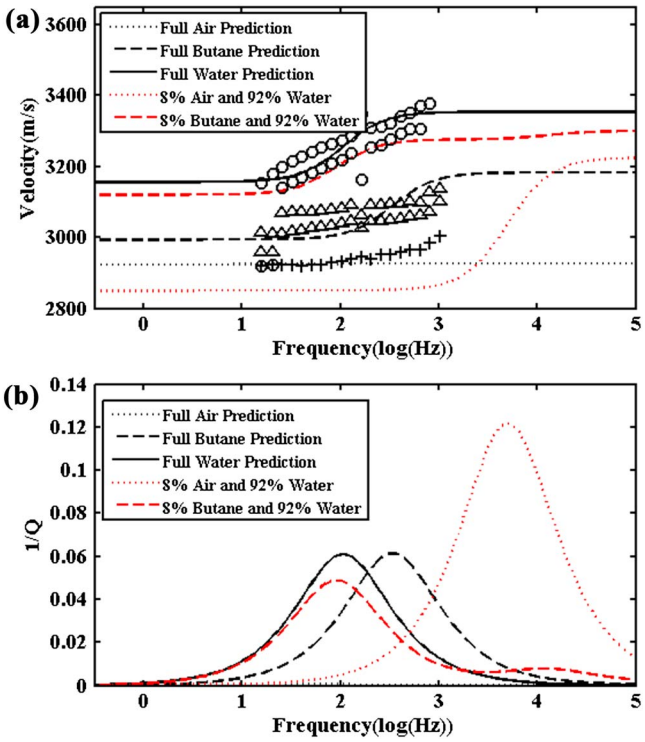

Figure 14. Fast compressional-wave (*P*1) (a) velocity and (b) attenuation as a function of frequency corresponding to the DDP model of the tight sandstone (sample TS). Low-frequency measurement data (using the technique in *Batzle et al.* [2006]) of compressional-wave velocity at full saturation in sample TS are comparatively given in Figure 14a, where the open circles, the unfilled triangles, and the crosses correspond to the three sets of data at full water, full butane, and full air saturation, respectively.

heterogeneity scale of each sample. Sample TS with mesoscopic heterogeneity shows strong seismic anelasticity when being fully saturated with water (see Figure 14). However, when air invades the water-saturated sample, the main anelasticity (dispersion and attenuation) tends to shift to the sonic band ($>10^3$ Hz).

4. Conclusions

A double double-porosity model for the Type-III anelasticity of compressional wave propagation has been presented by analyzing the overlapping effect of the two dissipation mechanisms. The first mechanism is wave-induced local fluid flow caused by fabric heterogeneity (Type-I anelasticity), and the second one is caused by fluid distribution heterogeneity (Type-II anelasticity). The governing wave equation is derived by using Hamilton's principle, based on the strain potential and kinetic energies and Biot's dissipation functions, where the coupled wave-induced fluid-flow process is modeled between the three sets of interfaces. The model allows for the most comprehensive description of compressional wave propagation and dissipation characteristics in highly complex in situ reservoir rocks, where the two types of heterogeneity coexist. Besides the traditional compressional wave, four slow waves are yielded by the theoretical model, corresponding to the Biot's sloshing/friction effect between the four phases of pore fluids and the main solid skeleton.

Three examples are given, corresponding to muddy siltstones, low-porosity clean dolomites, and tight sandstones, representing (1) submicroscopic heterogeneity of intrapore clay aggregates embedded in intergranular macropores, (2) microscopic heterogeneity of grain microcracks/contacts associated with pores between dolomite grains, and (3) mesoscopic heterogeneity of less consolidated sands inside the more consolidated skeleton of the tight sandstone. In all the three cases, the coupled wave-induced local fluid flow causes strong velocity dispersion and attenuation of the fast compressional waves, where more than one velocity inflection

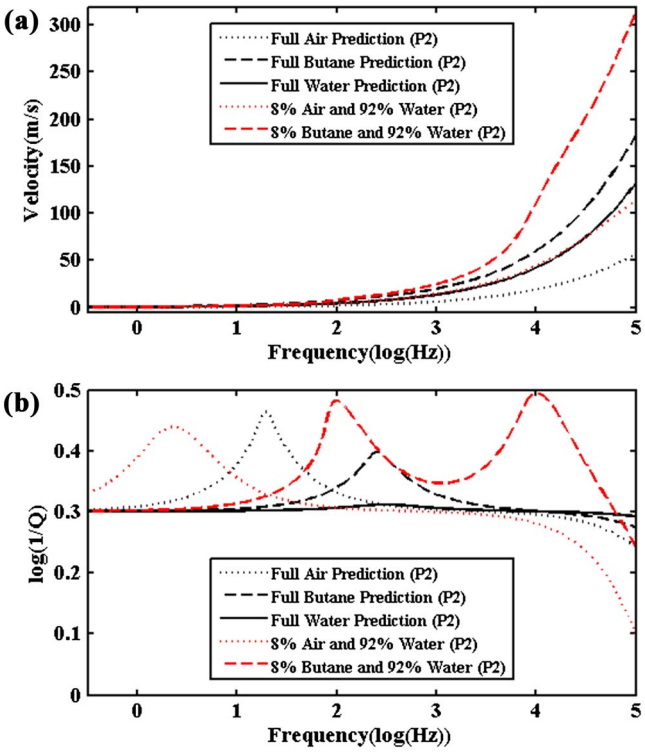

Figure 15. Phase (a) velocity and (b) attenuation of the Biot slow *P* wave *P*2 as a function of frequency corresponding to the DDP model of the fluid-saturated tight sandstone (sample TS).

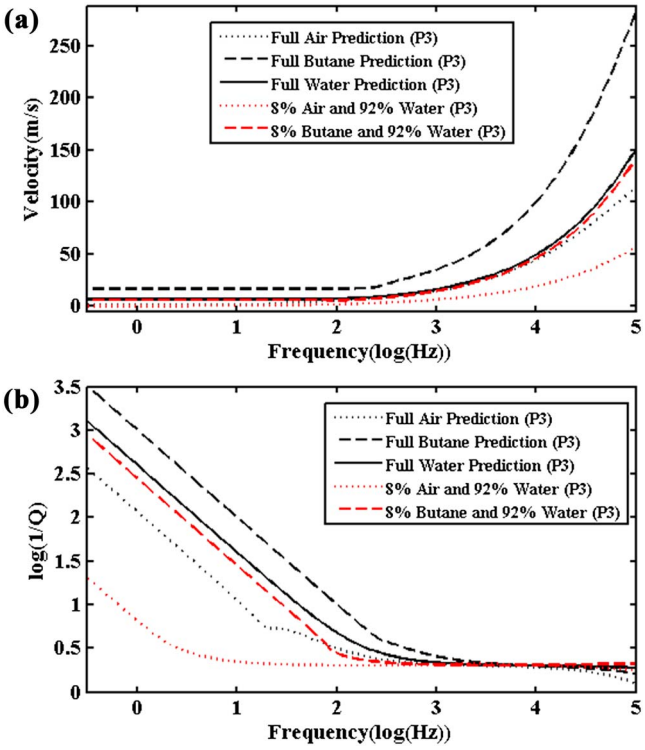

Figure 16. Phase (a) velocity and (b) attenuation of the Biot slow *P* wave *P*3 as a function of frequency corresponding to the DDP model of the fluid-saturated tight sandstone (sample TS).

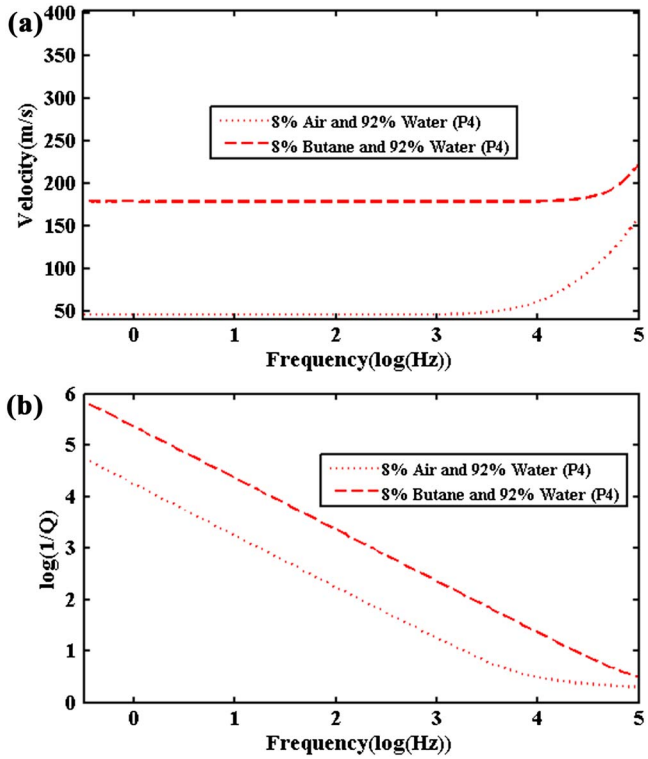

Figure 17. Phase (a) velocity and (b) attenuation of the Biot slow *P* wave *P*4 as a function of frequency corresponding to the DDP model of the fluid-saturated tight sandstone (sample TS).

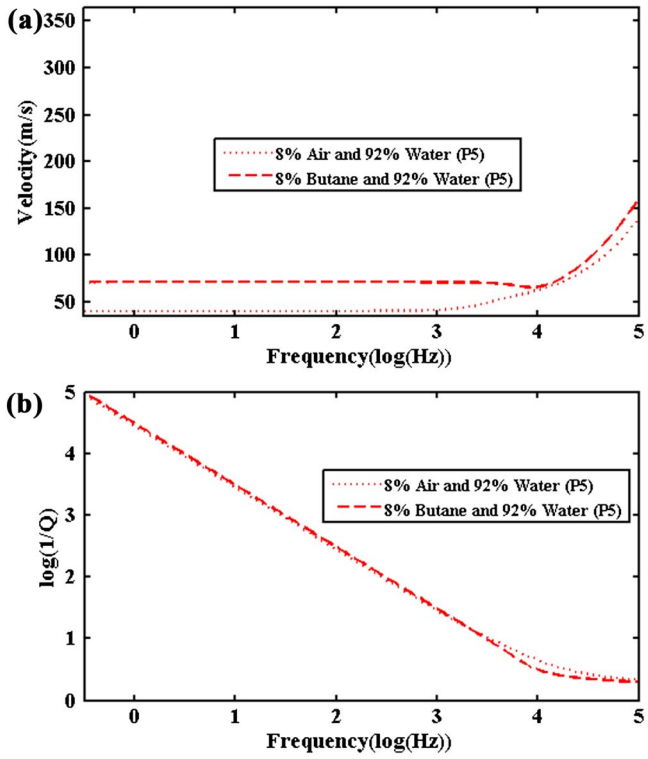

Figure 18. Phase (a) velocity and (b) attenuation of the Biot slow *P* wave *P*5 as a function of frequency corresponding to the DDP model of the fluid-saturated tight sandstone (sample TS).

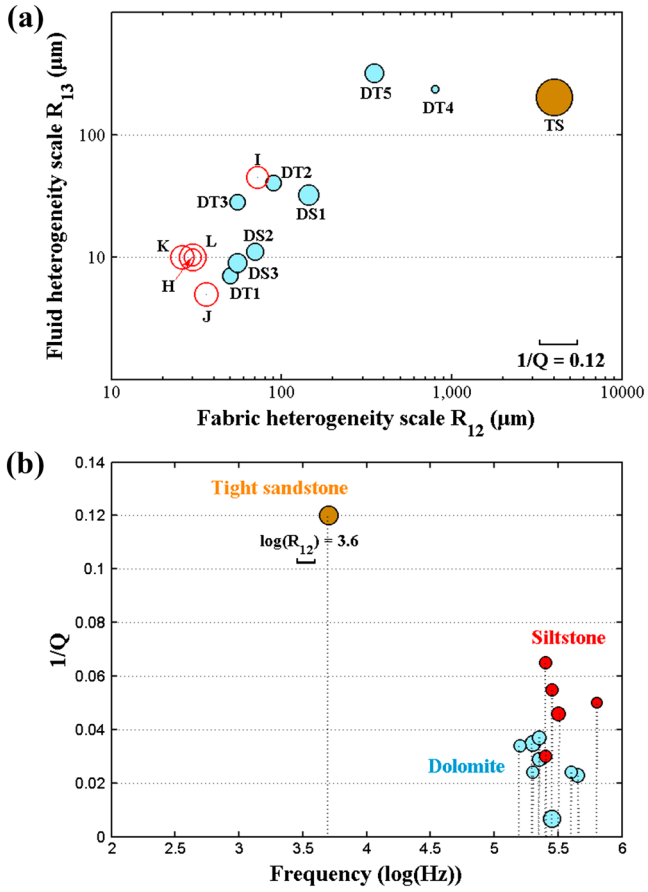

Figure 19. (a) Crossplot of rock-fabric heterogeneity size and fluid-pocket heterogeneity size in the 14 specimens. The diameter of the circles indicates the highest peak attenuation (1/*Q*) in each specimen (it is extracted from the modeling examples for all the partial saturation states). (b) Highest peak attenuation as a function of frequency for all the 14 specimens, where each characteristic frequency is labeled on the axis and the diameter of the circles indicate fabric heterogeneity size (log(R_{12})).

point (or attenuation peaks) can be observed, and broadening of the characteristic frequency band of anelasticity in comparison with the Type-I anelasticity. The mesoscopic case (3) gives the highest attenuation peak (in the seismic frequency band, very strong velocity dispersion can be observed in a comparison between the theoretical predictions and experimental data from low-frequency measurements), while the siltstone case (1) gives moderate values and the dolomite case (2) gives the lowest values. As is closely associated with the scale of fabric heterogeneity, wave anelasticity in siltstones, dolomites, and sandstones mainly occurs at 10^4–10^7 Hz (ultrasonic band), 10^3–10^7 Hz (mostly ultrasonic band; for oil-saturated dolomite, strong attenuation can be observed in the sonic band), and 10^1–10^3 Hz (seismic band), respectively. For the mesoscopic double-porosity model of the tight sandstone, the anelastic effects are strengthened when air invades each water-saturated porous component, moving the attenuation peaks and dispersion inflection points to the high frequencies.

In the present theory, the Hill average is adopted based on the fact that each fluid can be taken as the host fluid indistinctly, so that the compressional wave velocity can be estimated with arbitrary fluid-distribution geometries. Based on a single set of rock properties, the theoretical predictions of the relationship between compressional-wave velocity and saturation agree well with the ultrasonic experimental data.

We obtained high-quality ultrasonic waveforms in the siltstone specimens; however, the signal-to-noise ratio of waveforms in the carbonates is lower, which is a problem for estimating attenuation. The low-frequency attenuation estimates are not reliable for the data set of sample TS due to technical difficulties. Attenuation analysis in the different rock types will be performed in a future work.

Acknowledgments

This work is supported by the National Natural Science Foundation of China (41390454), the Distinguished Professor Program of Jiangsu Province, China, and the Fundamental Research Funds for the Central Universities, China. J. B. is grateful to the late M. Batzle for performing low-frequency measurements on tight sandstones in 2008 and also to his insightful comments in a personal discussion during the SEG Annual Meeting 2010 in Denver. Discussions with D.-H. Han were also helpful in 2014, when J. B. worked at the Rock Physics Laboratory of the University of Houston. Zhaobing Hao of the Institute of Geology and Geophysics, Chinese Academy of Sciences, helped performing ultrasonic experimental measurements on siltstones and carbonates. Review comments by the Editor, André Revil, Ludmila Adam, and an anonymous reviewer helped to improve the quality of this manuscript. Data associated with this article can be accessed by contacting Jing Ba at jba@hhu.edu.cn.

References

Adam, L., and T. Otheim (2013), Elastic laboratory measurements and modeling of saturated basalts, *J. Geophys. Res. Solid Earth*, *118*, 840–851, doi:10.1002/jgrb.50090.

Adam, L., M. L. Batzle, and I. Brevik (2006), Gassmann's fluid substitution and shear modulus variability in carbonates at laboratory seismic and ultrasonic frequencies, *Geophysics*, *71*, F173–F183.

Ba, J., J. M. Carcione, and J. Nie (2011), Biot-Rayleigh theory of wave propagation in double-porosity media, *J. Geophys. Res.*, *116*, B06202, doi:10.1029/2010JB008185.

Ba, J., J. M. Carcione, H. Cao, Q. Du, Z. Yuan, and M. Lu (2012), Velocity dispersion and attenuation of *P* waves in partially-saturated rocks: Wave propagation equations in double-porosity medium, *Chin. J. Geophys.*, *55*, 219–231.

Ba, J., L. Zhang, W. Sun, and H. Zhao (2014), Velocity field of wave-induced local fluid flow in double-porosity media, *Sci. China-Phys., Mech. Astron.*, *57*, 1020–1030.

Ba, J., J. Carcione, and W. Sun (2015a), Seismic attenuation due to heterogeneities of rock fabric and fluid distribution, *Geophys. J. Int.*, *202*, 1843–1847.

Ba, J., Q. Du, J. M. Carcione, H. Zhang, and T. M. Müller (2015b), *Seismic Exploration of Hydrocarbons in Heterogeneous Reservoirs: New Theories, Methods and Applications*, Elsevier Sci., Amsterdam.

Ba, J., J. Zhao, J. M. Carcione, and X. Huang (2016), Compressional wave dispersion due to rock matrix stiffening by clay squirt flow, *Geophys. Res. Lett.*, *43*, 6186–6195, doi:10.1002/2016GL069312.

Batzle, M. L., D.-H. Han, and R. Hofmann (2006), Fluid mobility and frequency-dependent seismic velocity—Direct measurements, *Geophysics*, *71*, N1–N9.

Best, A. I., and C. McCann (1995), Seismic attenuation and pore-fluid viscosity in clay-rich reservoir sandstones, *Geophysics*, *60*, 1386–1397.

Best, A. I., J. A. Priest, C. R. I. Clayton, and E. V. L. Rees (2013), The effect of methane hydrate morphology and water saturation on seismic wave attenuation in sand under shallow sub-seafloor conditions, *Earth Planet. Sci. Lett.*, *368*, 78–87.

Biot, M. A. (1956), Theory of propagation of elastic waves in a fluid-saturated porous solid. I. Low-frequency range, *J. Acoust. Soc. Am.*, *28*, 168–178.

Biot, M. A. (1962), Mechanics of deformation and acoustic propagation in porous media, *J. Appl. Phys.*, *33*, 1482–1498.

Biot, M. A., and D. G. Willis (1957), The elastic coefficients of the theory of consolidation, *J. Appl. Mech.*, *24*, 594–601.

Cadoret, T., D. Marion, and B. Zinszner (1995), Influence of frequency and fluid distribution on elastic wave velocities in partially saturated limestones, *J. Geophys. Res.*, *100*, 9789–9803, doi:10.1029/95JB00757.

Carcione, J. M. (2014), *Wave Fields in Real Media. Theory and Numerical Simulation of Wave Propagation in Anisotropic, Anelastic, Porous and Electromagnetic Media*, 3rd ed., Elsevier Sci., Amsterdam.

Carcione, J. M., and B. Gurevich (2011), Differential form and numerical implementation of Biot's poroelasticity equations with squirt dissipation, *Geophysics*, *76*, N55–N64.

Caspari, E., T. M. Müller, and B. Gurevich (2011), Time-lapse sonic logs reveal patchy CO_2 saturation in-situ, *Geophys. Res. Lett.*, *38*, L13301, doi:10.1029/2011GL046959.

Chapman, M. (2003), Frequency-dependent anisotropy due to meso-scale fractures in the presence of equant porosity, *Geophys. Prospect.*, *51*, 369–379.

Ciz, R., B. Gurevich, and M. Markov (2006), Seismic attenuation due to wave-induced fluid flow in a porous rock with spherical heterogeneities, *Geophys. J. Int.*, *165*, 957–968.

Dutta, N. C., and H. Odé (1979), Attenuation and dispersion of compressional waves in fluid-filled porous rocks with partial gas saturation (White model)—Part I: Biot theory, *Geophysics*, *44*, 1777–1788.

Dvorkin, J., and A. Nur (1993), Dynamic poroelasticity: A unified model with the squirt and the Biot mechanisms, *Geophysics*, *58*, 524–533.

Dvorkin, J., R. Nolen-Hoeksema, and A. Nur (1994), The squirt-flow mechanism: Macroscopic description, *Geophysics*, *59*, 428–438.

Gassmann, F. (1951), Uber die Elastizat Poroser Medien, *Vierteljahrsschr. Naturforsch. Ges. Zurich*, *96*, 1–23.

Guo, M., L. Fu, and J. Ba (2009), Comparison of stress-associated coda attenuation and intrinsic attenuation from ultrasonic measurements, *Geophys. J. Int.*, *178*, 447–456.

Gurevich, B., and S. L. Lopatnikov (1995), Velocity and attenuation of elastic waves in finely layer porous rocks, *Geophys. J. Int.*, *121*, 933–947.

Hao, Z., J. Ba, L. Zhang, Q. Zeng, R. Jiang, J. Liu, W. Qian, W. Tan, and W. Chen (2016), Rock physics inversion workflow on reservoir parameters: A case study of seismic hydrocarbon detection in large-area tight dolomite reservoirs, *J. Seism. Explor.*, *25*, 561–588.

Hashin, Z., and S. Shtrikman (1963), A variational approach to the theory of the elastic behaviour of multiphase materials, *J. Mech. Phys. Solids*, *11*, 127–140.

Johnson, D. L. (1986), Recent developments in the acoustic properties of porous media, in *Frontiers in Physical Acoustics XCIII*, edited by D. Sette, pp. 255–290, Elsevier, New York.

Johnson, D. L. (2001), Theory of frequency dependent acoustics in patchy saturated porous media, *J. Acoust. Soc. Am.*, *110*, 682–694.

King, M. S., and J. R. Marsden (2002), Velocity dispersion between ultrasonic and seismic frequencies in brine-saturated reservoir sandstones, *Geophysics*, *67*, 254–258.

Lebedev, M., J. Toms, B. Clennell, M. Pervukhina, V. Shulakova, L. Paterson, T. M. Müller, B. Gurevich, and F. Wenzlau (2009), Direct laboratory observation of patchy saturation and its effect on ultrasonic velocities, *Leading Edge*, *28*, 24–27.

Lopes, S., M. Lebedev, T. M. Müller, M. B. Clennell, and B. Gurevich (2014), Forced imbibition into a limestone: Measuring *P*-wave velocity and water saturation dependence on injection rate, *Geophys. Prospect.*, *62*, 1126–1142.

Marketos, G., and A. I. Best (2010), Application of the BISQ model to clay squirt flow in reservoir sandstones, *J. Geophys. Res.*, *115*, B06209, doi:10.1029/2009JB006495.

Mavko, G. M., and A. Nur (1975), Melt squirt in the asthenosphere, *J. Geophys. Res.*, *80*, 1444–1448.

Mavko, G. M., and A. Nur (1978), The effect of nonelliptical cracks on the compressibility of rocks, *J. Geophys. Res.*, *83*, 4459–4468.

Mavko, G. M., and A. Nur (1979), Wave attenuation in partially saturated rocks, *Geophysics*, *44*, 161–178.

Müller, T. M., and B. Gurevich (2005), A first-order statistical smoothing approximation for the coherent wave field in random porous media, *J. Acoust. Soc. Am.*, *117*, 1795–1805.

Müller, T. M., B. Gurevich, and M. Lebedev (2010), Seismic wave attenuation and dispersion resulting from wave-induced flow in porous rocks—A review, *Geophysics*, *75*, 75A147–75A164.

Norris, A. N. (1993), Low-frequency dispersion and attenuation in partially saturated rocks, *J. Acoust. Soc. Am.*, *94*, 359–370.

Pride, S. R., J. G. Berryman, and J. M. Harris (2004), Seismic attenuation due to wave-induced flow, *J. Geophys. Res.*, *109*, B01201, doi:10.1029/2003JB002639.

Quintal, B., H. Steeb, M. Frehner, S. M. Schmalholz, and E. H. Saenger (2012), Pore fluid effects on *S*-wave attenuation caused by wave-induced fluid flow, *Geophysics*, *77*, L13–L23.

Rayleigh, L. (1917), On the pressure developed in a liquid during the collapse of a spherical cavity, *Philos. Mag.*, *34*, 94–98.

Rubino, G. J., and K. Holliger (2012), Seismic attenuation and velocity dispersion in heterogeneous partially saturated porous rocks, *Geophys. J. Int.*, *188*, 1088–1102.

Spencer, J. W., and J. Shine (2016), Seismic wave attenuation and modulus dispersion in sandstones, *Geophysics*, *81*, D211–D231.

Sun, W., J. Ba, T. M. Müller, J. M. Carcione, and H. Cao (2015), Comparison of *P*-wave attenuation models of wave-induced flow, *Geophys. Prospect.*, *63*, 378–390.

Sun, W., J. Ba, and J. M. Carcione (2016), Theory of wave propagation in partially saturated double-porosity rocks: A triple-layer patchy model, *Geophys. J. Int.*, *205*, 22–37.

Tisato, N., and B. Quintal (2014), Laboratory measurements of seismic attenuation in sandstone: Strain versus fluid saturation effects, *Geophysics*, *79*, WB9–WB14.

Toms, J., T. M. Müller, R. Ciz, and B. Gurevich (2006), Comparative review of theoretical models for elastic wave attenuation and dispersion in partially saturated rocks, *Soil Dyn. Earthquake Eng.*, *26*, 548–565.

White, J. E. (1975), Computed seismic speeds and attenuation in rocks with partial gas saturation, *Geophysics*, *40*, 224–232.

White, J. E., N. Mihailova, and F. Lyakhovitsky (1975), Low-frequency seismic waves in fluid-saturated layered rocks, *J. Acoust. Soc. Am.*, *57*(S1), S30–S30.

Zhang, L., J. Ba, W. Yin, W. Sun, and J. Tang (2017), Seismic wave propagation equations in conglomerate reservoir: A triple-porosity structure model, *Chin. J. Geophys.*, *60*, doi:10.6038/cjg20170201.

Zhou, S., Y. Wei, Z. Hao, and W. Huang (2012), Experiment research and application of fluid sensitive attributes based on the pre-stack inversion, *Chin. J. Geophys.*, *55*, 1985–1992.